Article │ Received 23 February 2025; Accepted 21 May 2025; Published 19 June 2025
https://doi.org/10.55092/sc20250013

Bond behavior of FRP bars in concrete under reversed cyclic loading: an experimental study

Bo Li[1], Dong Li[1], Fengjuan Chen[1,2,3,*], Liu Jin[1] and Xiuli Du[1]

[1] The key laboratory of Urban Security and Disaster Engineering, Beijing University of Technology, Beijing 100124, China
[2] Chongqing Research Institute of Beijing University of Technology, Chongqing 401121, China
[3] Nuclear Industry X Intelligence Laboratory, Beijing University of Technology, Beijing 100124, China

*Corresponding author; Email: fengjuanchen@bjut.edu.cn.

Highlights:

- Investigates cyclic bond behavior of CFRP, GFRP, and BFRP bars in concrete.
- Quantifies effects of bar diameter, embedment length, and concrete strength.
- Proposes a unified bond stress-slip model with hysteresis under cyclic loading.
- Reveals interfacial degradation mechanisms critical for seismic FRP design.

Abstract: This study addresses gaps in understanding cyclic bond behavior of fiber reinforced polymer (FRP) bars. By analyzing carbon fiber reinforced polymer (CFRP), glass fiber reinforced polymer (GFRP), and basalt fiber reinforced polymer (BFRP) bars under reversed cyclic loading, it quantifies how bar diameter, embedment length, concrete strength, and rib geometry govern initial stiffness, unloading strength, friction resistance, and energy dissipation. A unified bond stress-slip constitutive model and hysteresis framework are established, elucidating interfacial degradation mechanisms and providing critical insights for optimizing seismic-resistant FRP-concrete structural design.

Keywords: bond behavior; fiber reinforced polymer; reversed cyclic loading; bond stress-slip constitutive model

1. Introduction

Civil engineering structures, such as buildings, bridges, and tunnels, are highly susceptible to seismic damage, resulting in considerable economic losses and endangering the safety of workers, residents, and passersby. Accurate estimation of the bond properties between the reinforcing bars and concrete is crucial in seismic analysis, as this bond facilitates the transfer of internal forces from concrete to reinforcing bars, thus ensuring structural integrity under seismic loading conditions [1–4]. While traditional steel reinforcement has been extensively studied, the increasing application of fiber-reinforced polymer (FRP) bars in civil engineering has led to a shift in research focus towards understanding the bond behavior of

FRP-reinforced concrete structures. In addition to conventional FRP-concrete systems, recent studies have explored innovative material combinations, such as the bond behavior between glass fiber-reinforced polymer (GFRP) bars and seawater sea-sand fiber-reinforced ultra-high strength concrete (UHSSC), owing to their enhanced corrosion resistance and sustainability in marine environments [5–7]. These investigations underscore the evolving complexity of interfacial mechanics in aggressive service conditions and highlight the limitations of traditional bond models when applied to these advanced composites.

Research on the bond properties of FRP bars under cyclic loading remains limited, with most experimental studies indicating a reduction in bond strength under such conditions. Several analytical bond stress-slip models have been proposed based on experimental data [5–14] and fracture theory [15–17]. However, these models tend to be empirical or semi-empirical, particularly for FRP bars, and often provide only a general understanding of bond stress behavior under applied loading. More importantly, they fail to explain the sources of data dispersion, the phenomenon of shear stress reversal, and the underlying bonding and debonding mechanisms. Moreover, they rarely account for the effects of evolving damage at the mesoscopic scale. These gaps highlight the need for further research, particularly at the mesoscopic level, to better understand the bond behavior of FRP-reinforced concrete systems. Emerging directions, including the use of distributed fiber optic sensors to monitor localized bond degradation [18] and micromechanical simulations of FRP-concrete interfaces under multi-axial stress states [19], offer promising tools for bridging this gap.

In recent years, as the use of FRP bars in concrete components has become increasingly prevalent in engineering applications [20], greater attention has been paid to the influence of mesoscopic factors on the bond properties between FRP bars and concrete. These factors include bar geometry [21], surface conditions [22], confinement pressure [23], concrete compressive strength [24–25], bar diameter [26–27], embedment length [28–29], temperature variations [30–31], and environmental conditions [32–33]. In particular, recent studies have provided deeper insights into the specific impacts of bonded length and bar diameter on FRP-concrete bond strength, addressing the limitations of earlier empirical findings [34–36]. Notably, the interaction between FRP bars and advanced concrete matrices such as seawater sea-sand UHSSC introduces unique challenges due to the combined effects of salt crystallization, matrix densification, and fiber hybridization on interfacial mechanics [37].

Shen *et al.* [38] demonstrated a strong correlation between bond stress at the FRP-concrete interface and factors such as bar diameter, embedment length, and concrete strength. Their study on basalt fiber-reinforced polymer (BFRP)-reinforced concrete showed that reducing the bar diameter and embedment length while increasing concrete strength significantly enhanced bond strength. Gong *et al.* [39] and Akbas *et al.* [40] further confirmed this trend, observing that increasing embedment length consistently reduced average bond stress, regardless of the matrix strength. More recently, studies such as Zhang *et al.* [41] and Rolland *et al.* [42] have provided experimental verification and numerical modeling approaches that reinforce these observations, offering enhanced predictive capabilities for different FRP types and loading regimes. This suggests that bond performance is governed by a coupled mechanism of mechanical interlock and interfacial adhesion, sensitive to both bar geometry and surrounding concrete composition.

Research on the effect of cyclic loading has also shown significant impacts on bond behavior. Lee *et al.* [43] investigated the influence of cyclic loading on the bond performance of GFRP-reinforced concrete, finding that both the surface properties of the bars and the number of loading cycles played a

significant role in bond strength. Akbas *et al.* [44] similarly observed that cyclic loading reduced the bond capacity of FRP-reinforced concrete elements. Recent experimental work on GFRP-reinforced seawater sea-sand UHSSC further demonstrated that wet-dry cycles accelerated bond degradation, leading to interfacial weakening modes distinct from those in traditional concrete systems [5]. Additionally, Xie *et al.* [45] demonstrated that rib height, width, and spacing have a substantial impact on bond strength between GFRP bars and concrete. An increase in the deformation coefficient (the ratio of rib width to spacing) significantly enhanced bond strength and gradually shifted the failure mode from pull-out to concrete splitting. Liu *et al.* [46] confirmed these findings for BFRP-reinforced concrete, suggesting that a rib spacing of 12 mm and a rib width of 2.5 mm were optimal for maximizing bond strength while maintaining moderate slip. Among different rib shapes, round ribbed BFRP bars exhibited the highest bond strength. Similarly, Achillides *et al.* [20] emphasized the importance of bar shape in determining bond stress, noting that square bars provided 25% greater bond strength compared to round bars, likely due to the wedging effect created by the sharp edges of square bars.

Nevertheless, it should be noted that the application of FRP bars in structures subjected to high seismic actions remains limited and controversial. Due to their linear elastic behavior until failure and the lack of yielding mechanisms, FRP-reinforced structures inherently have lower energy dissipation capacities during strong seismic events [47]. Therefore, FRP bars are more appropriately applied in regions with moderate to low seismic risk, or in infrastructures where durability and corrosion resistance are prioritized over seismic ductility, such as marine structures, coastal bridges, parking garages, and offshore platforms [7].

Despite these valuable insights, existing studies on mesoscopic factors influencing bond characteristics have limitations in terms of scope and quantity. While some progress has been made in explaining data dispersion and shear stress reversal phenomena, a comprehensive understanding of the underlying bonding and debonding mechanisms remains elusive. Moreover, the limited number of studies and the empirical nature of existing models hinder the development of accurate bond constitutive equations for FRP-reinforced concrete systems. Consequently, future research should prioritize an in-depth investigation of FRP-concrete bond behavior under cyclic loading conditions, with a particular emphasis on unifying structural descriptors across all types of FRP-reinforced concrete systems.

This study addresses these limitations through a systematic investigation of cyclic bond behavior in FRP-reinforced concrete, encompassing CFRP, GFRP, and BFRP bars. By experimentally analyzing the effects of bar diameter, embedment length, concrete strength, and rib geometry, we quantify their influence on initial stiffness, unloading strength, friction resistance, and energy dissipation. A novel unified bond stress-slip constitutive model is proposed, which integrates mesoscopic interactions and cyclic degradation mechanisms. This model not only elucidates the origins of data dispersion and shear stress reversal but also provides a predictive tool for optimizing FRP-reinforced systems in seismic and durability-focused applications. The findings contribute both to the advancement of fundamental understanding and to the formulation of design strategies for FRP-reinforced structures, particularly in service environments where corrosion resistance and moderate seismic resilience are critical design considerations.

2. Experimental setup

2.1. Preparation of the test specimens

Prior to bond testing, the mechanical properties of CFRP, BFRP, and GFRP bars were determined through uniaxial tensile tests in accordance with ASTM D7205 [48]. Three specimens per FRP type were tested to ensure statistical reliability. As summarized in Table 1, CFRP bars exhibited the highest tensile strength (f_u = 2028 MPa), elastic modulus (E = 73.4 GPa) and Ultimate tensile strain ($\epsilon_{ult} = 1.40\%$), followed by BFRP (f_u = 1373 MPa, E = 34.3 GPa, $\epsilon_{ult} = 4.0\%$) and GFRP (f_u = 759 MPa, E = 20 GPa, $\epsilon_{ult} = 3.80\%$). The mechanical characterization of concrete was performed following GB/T 50081–2019 [49], with compressive and tensile strength results for C30 and C60 concrete summarized in Table 2. The average compressive strengths (f_{cu}) were 36.27 MPa (C30) and 62.47 MPa (C60), while splitting tensile strengths (f_t) reached 2.8 MPa (C30) and 5.2 MPa (C60), ensuring compliance with design specifications.

Table 1. Properties of FRP bars.

Types of FRP bars	d (mm)	Tensile strength (MPa)	Elasticity modulus (GPa)	Ultimate tensile strain (%)
BFRP	16	1373	34.3	4
CFRP	16	2028	73.4	1.40
GFRP	16	759	20.0	3.80

Table 2. Mix proportions and properties of concrete.

Concrete Type	Water (%)	Cement (%)	Fine Aggregate (%)	Coarse Aggregate (%)	Fly ash (%)	Compressive Strength (MPa)	Splitting Tensile Strength (MPa)
C30	7.07	13.11	32.37	42.84	3.93	36.27	2.8
C60	7.11	10.65	32.39	44.72	4.53	62.47	5.2

The experimental program utilized 150 mm^3 concrete cubes with 750 mm-long FRP bars. Embedment lengths were set at 3 d, 5 d, and 8 d (where d = nominal bar diameter), as detailed in Table 3 under the nomenclature "Bar type–Concrete strength–Diameter-Embedment length." To prevent cement infiltration, unembedded sections of FRP bars were shielded by PVC sleeves, while loading ends were secured with epoxy-filled steel collars (Figure 1). Each configuration was tested five times to mitigate operational variability, with reported values representing averaged measurements.

The choice of relatively short embedment lengths was deliberate and aimed to ensure that pullout failure dominated the bond behavior, thereby avoiding premature bar rupture or concrete splitting failures. Such a setup allows for the precise characterization of the fundamental interfacial stress transfer mechanisms, isolated from complex global structural effects. While the selected embedment lengths do not replicate the full development lengths typically encountered in large-scale structural applications, they are consistent with standard practice in bond mechanics studies and provide essential data for the development and validation of local bond-slip constitutive models [50]. This targeted approach is critical for

advancing predictive capabilities and informing design guidelines for FRP-reinforced concrete systems.

Table 3. Specimen parameters.

Specimen	d (mm)	L (mm)	Concrete Grade	f_{cu} (MPa)
BFRP-C30-10-5d	10	50	C30	36.67
BFRP-C30-16-5d	16	80	C30	36.67
BFRP-C30-20-5d	20	100	C30	36.67
BFRP-C30-16-3d	16	48	C30	36.67
BFRP-C30-16-8d	16	128	C30	36.67
BFRP-C60-16-5d	16	80	C60	62.47
CFRP-C30-10-5d	10	50	C30	36.67
CFRP-C30-16-5d	16	80	C30	36.67
CFRP-C30-20-5d	20	100	C30	36.67
CFRP-C30-16-3d	16	48	C30	36.67
CFRP-C30-16-8d	16	128	C30	36.67
CFRP-C60-16-5d	16	80	C60	62.47
GFRP-C30-10-5d	10	50	C30	36.67
GFRP-C30-16-5d	16	80	C30	36.67
GFRP-C30-20-5d	20	100	C30	36.67
GFRP-C30-16-3d	16	48	C30	36.67
GFRP-C30-16-8d	16	128	C30	36.67
GFRP-C60-16-5d	16	80	C60	62.47

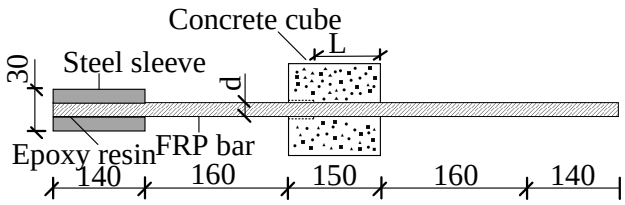

Figure 1. Schematic drawing of the specimen.

Interfacial bond behavior was critically influenced by FRP surface characteristics (Figure 2). CFRP bars displayed regular rib patterns with low rib height-to-spacing ratios ($\frac{\Delta h}{l} = 0.42$, where $\Delta h = h^2 - h^1$represents the rib height and l is the rib spacing), resulting in diminished mechanical interlock due to smooth carbon and epoxy interfaces. Conversely, BFRP bars exhibited irregular wavy textures ($\frac{\Delta h}{l} = 0.50$, where $\Delta h = h_2 - h_1$ represents the rib height and l is the rib spacing) and higher roughness, enhancing micro-interlocking and frictional resistance. GFRP surfaces featured periodic ribs ($\frac{\Delta h}{l} = 0.46$, where $\Delta h = h_2 - h_1$ represents the rib height and l is the rib spacing) prone to localized deformation under stress, with intermediate roughness, which favors frictional dissipation-dominated slip behavior. These distinct surface characteristics fundamentally govern the stress transfer mechanisms and damage evolution pathways of FRP bars within concrete matrices.

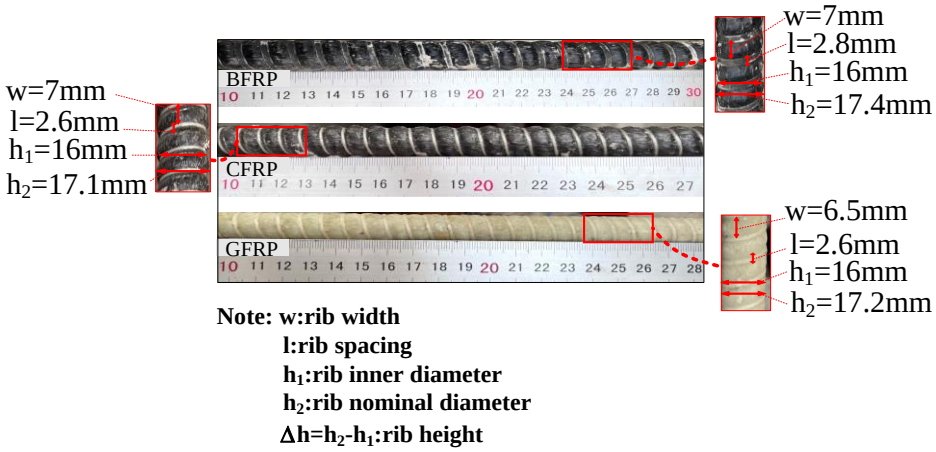

Figure 2. Surface characteristics of three different FRP bars (d = 16 mm).

2.2. Test device and loading scheme

The bonding test was conducted using a servo-hydraulic testing machine (MTS), as shown in Figure 3(a). The counter-force frame was constructed using three steel plates, labeled 1#, 2#, and 3#, which were firmly attached to a fixed base through the use of twenty-four 6# screws and four threaded steel rods. This robust setup ensured stability and minimized any movement during the test. Prior to the test, the FRP-reinforced concrete cube was carefully positioned between steel plates 1# and 2#, and securely fastened using adjusting nuts. This arrangement was crucial for maintaining the specimen's alignment and preventing any displacement during loading, ensuring accurate test results.

Displacement-controlled loading was employed throughout the testing, with the stroke of the servo-hydraulic machine used as the control input. To independently monitor the bond-slip response, slip measurements were recorded at both the loaded and free ends. Two cable-type displacement transducers were installed at each end of the FRP bar to precisely capture the relative displacement between the bar and the surrounding concrete. In accordance with standard bond-slip definitions, the slip measured at the loaded end was adopted for constructing the $\tau - s$ (bond stress-slip) relationships. The configuration of the displacement sensors is schematically presented in Figure 3(a), wherein the transducers were rigidly attached to the FRP bar and anchored to the reaction frame to minimize extraneous movements and ensure accurate slip measurements.

The loading rate was set at 0.05 mm/s to allow for gradual application of force. The loading was continuously applied until the specimens failed due to bond stress-slip, which was the primary failure mode under the given conditions [50]. The loading scheme, including the number of loading cycles and the amplitude of the applied force, is shown in Figure 3(b). A displacement-controlled loading scheme with an amplitude of $\pm$ 15 mm was carefully selected to replicate realistic seismic displacement demands while ensuring a controlled progression of damage. This amplitude was determined through preliminary monotonic pull-out tests, corresponding to 80%–90% of the critical slip value at the onset of bond strength degradation, thereby capturing both elastic interfacial behavior and post-peak frictional resistance evolution [39]. Three loading cycles were applied to characterize the stabilization of residual slip and the reduction in stiffness, while minimizing excessive cumulative damage that could obscure failure mode identification—a methodology consistent with ASTM D7205 guidelines for FRP bond testing under cyclic loads [48].

(a)

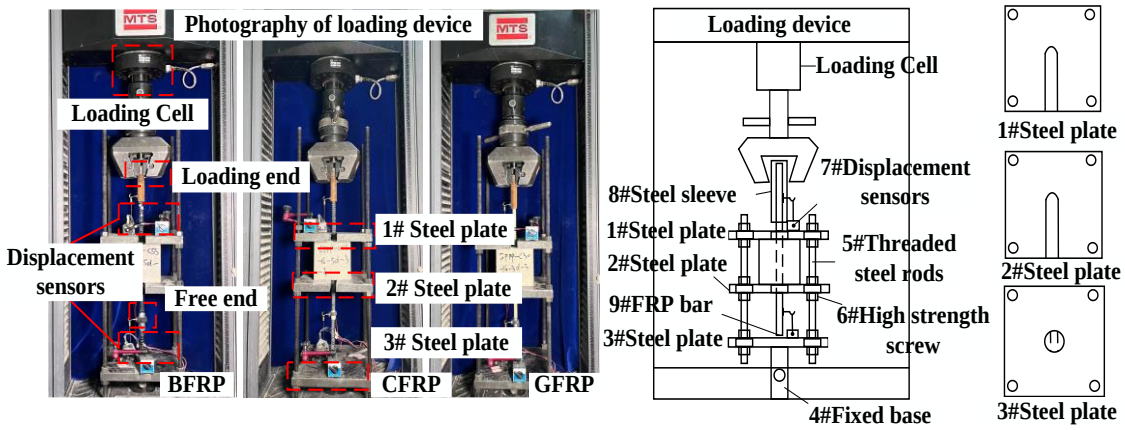

(b)

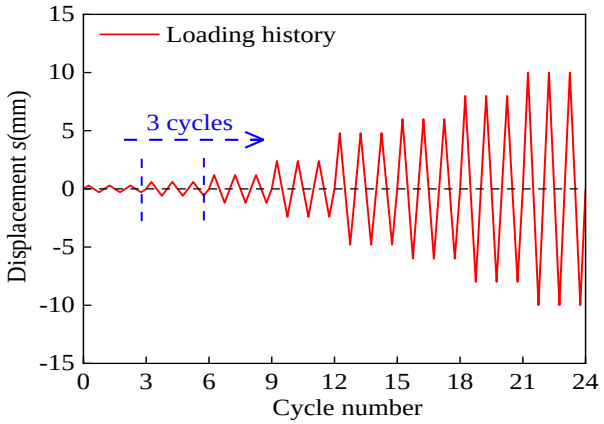

Figure 3. Test design. **(a)** Test setup; **(b)** Loading scheme.

In addition, symmetric displacement cycles were adopted to simulate bidirectional seismic actions, allowing the investigation of shear stress reversal and asymmetric damage accumulation at the FRP-concrete interface. These phenomena are critical for seismic design but are often overlooked in unidirectional loading protocols [43]. This comprehensive test setup, designed to simulate dynamic and seismic loading conditions, provides reliable quantification of key degradation parameters, including energy dissipation capacity, unloading stiffness evolution, and slip recovery rates, all of which are crucial for validating the proposed constitutive model under displacement-driven seismic conditions.

3. Bond characteristics of CFRP-, BFRP- and GFRP- reinforced concrete

This study investigates the interfacial characteristics of CFRP-, BFRP-, and GFRP-reinforced concrete through an integrated experimental-numerical framework. The analytical approach builds upon the authors' previously validated cyclic bond-slip constitutive model for CFRP bars [51], which explicitly accounts for mesoscopic interfacial features (e.g., rib geometry, matrix microcracking). Experimental results are categorized into two groups for systematic comparison: (1) Group 1: CFRP-reinforced concrete systems; (2) Group 2: BFRP/GFRP-reinforced concrete systems.

The bond stress τ is calculated using:

$$\tau = \frac{F}{\pi \cdot d \cdot L} \quad (1)$$

with τ the average bond stress (MPa); F the applied bond force (N); L the bonding length (mm) and d the rebar diameter (mm).

It is acknowledged that the $\tau - s$ law theoretically represents a local constitutive relationship associating the slip at a specific point with the interfacial shear stress at the same location. However, in practical experimental settings, direct measurement of local bond stress along the embedded length is challenging due to limitations in sensor resolution and concrete disturbance. Therefore, following standard practice in bond research [50], the average bond stress is widely adopted as a surrogate measure. In this study, the short embedment lengths (3 d–8 d) were carefully selected to promote approximately uniform stress distribution along the bonded region, thereby minimizing the gradient of bond stress and enabling the average bond stress to closely approximate the local behavior. This approach has been validated in prior experimental [52–53] investigations and provides a practical and reliable basis for establishing the bond-slip relationships required for mesoscale modeling and structural analysis.

3.1. Experimental results for CFRP bars

Four distinct failure modes were observed during testing (Figure 4(a)): (1) localized concrete damage near the bar ribs, (2) pullout failure, (3) splitting failure, and (4) reinforcement fracture. The failure mode is mainly correlated with rib geometry parameters (rib height, rib spacing, and the ratio of rib width to rib spacing), consistent with micromechanical analyses in [51].

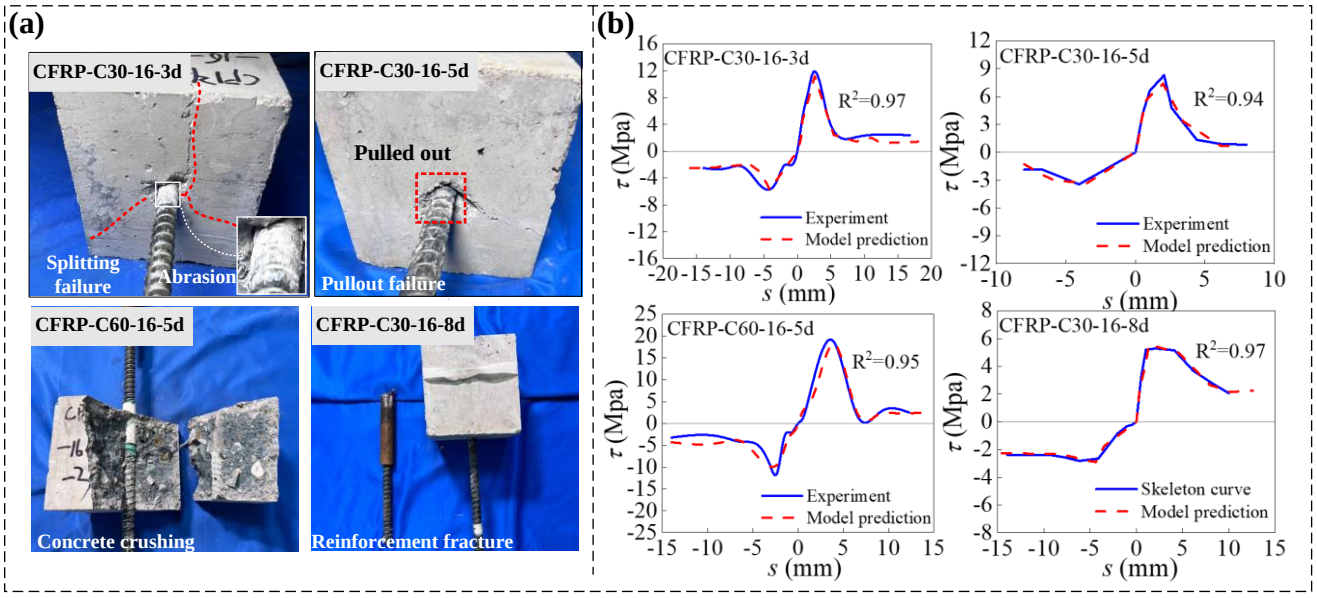

Figure 4. CFRP reinforcement specimens. **(a)** Damage forms; **(b)** Verification of constitutive equations.

The "established constitutive model" is a cyclic bond-slip model developed to simulate the interaction between CFRP bars and concrete under cyclic loading. This model integrates geometric factors (such as rib geometry and spacing) to predict the bond stress-slip behavior under cyclic loading conditions.

The validation procedure for this model involved comparing the numerical predictions of bond stress-slip behavior with experimental data obtained from cyclic pull-out tests. In the cyclic pull-out tests, the bond stress was measured under repeated loading and unloading cycles, simulating real-world loading conditions. This experimental setup was used to validate the model's ability to accurately predict the bond stress-slip behavior under cyclic loading, which is the primary focus of this study.

The comparison between experimental and numerical results from cyclic pull-out tests was crucial for model validation. The experimental data, including the cyclic loading and unloading curves, were used to assess the model's performance in simulating the complete bond stress-slip response, including the maximum bond stress, unloading stiffness, and the degradation of bond strength with repeated loading cycles. The results from the numerical predictions were compared with the experimental hysteresis curves, which confirmed that the model accurately captures the bond stress-slip behavior under cyclic loading.

Figure 4(b) illustrates the validation of the established constitutive model by comparing the experimental and numerical skeleton curves. The experimental data from the cyclic pull-out tests were used to construct the skeleton curves, which show the bond stress as a function of slip. The numerical results from the model's predictions were then compared with the experimental skeleton curves, demonstrating a strong correlation. This comparison confirmed that the model accurately predicts the bond stress-slip behavior of CFRP bars under cyclic loading conditions.

Regarding the procedure for deriving the slip s, the slip values reported in the horizontal axis of Figure 4(b) were derived from experimental displacement measurements at the FRP–concrete interface. Specifically, the slip s was calculated as the relative displacement between the FRP bar and the surrounding concrete at the bond interface. Displacement transducers and strain gauges were used to measure the displacement of the FRP bar during each loading cycle. The slip was then obtained by subtracting the displacement of the surrounding concrete from that of the bar, allowing for the accurate determination of slip at each load step. These slip values were used to construct the skeleton curves, which were then compared with the model's predictions for validation.

3.2. Experimental results for BFRP-and GFRP-reinforced concrete

After the bond stress-slip characteristics between CFRP bars and concrete were validated through experiments, a series of tests was conducted to examine the bond behavior between BFRP/GFRP bars and concrete. The goal was to identify a unified stress-slip relationship applicable to CFRP, BFRP, and GFRP bars. As shown in Figure 5, the failure modes of BFRP-reinforced specimens are primarily splitting and pull-out failures, whereas GFRP-reinforced specimens predominantly exhibit pull-out failure.

As illustrated in Figure 6, the bonding behavior of GFRP and BFRP bars follows a similar pattern. The maximum bond stress decreases as the bar diameter and embedment length increase, but it rises with higher concrete strength. For example, when the compressive strength of the concrete was C30 and the diameter of the GFRP bar was 16 mm, the maximum bond stress for specimens with embedment lengths of 48 mm, 80 mm, and 128 mm was 7.86 MPa, 5.09 MPa, and 4.95 MPa, respectively. Specifically, the maximum bond stress for specimens with embedment lengths of 3 d (48 mm) and 5 d (80 mm) increased by 37.02% and 2.75% compared to those with an embedment length of 8 d (128 mm), the bond stress-slip hysteresis curves for each individual working condition are shown in Appendix A.

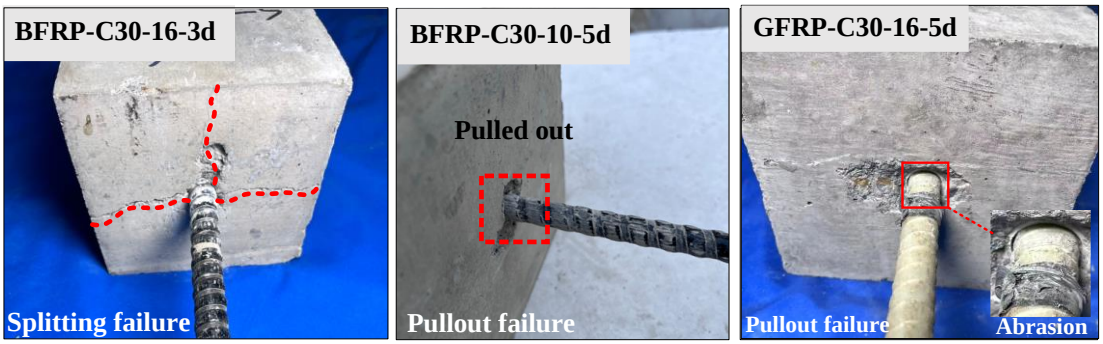

Figure 5. Damage forms of BFRP and GFRP reinforced specimens.

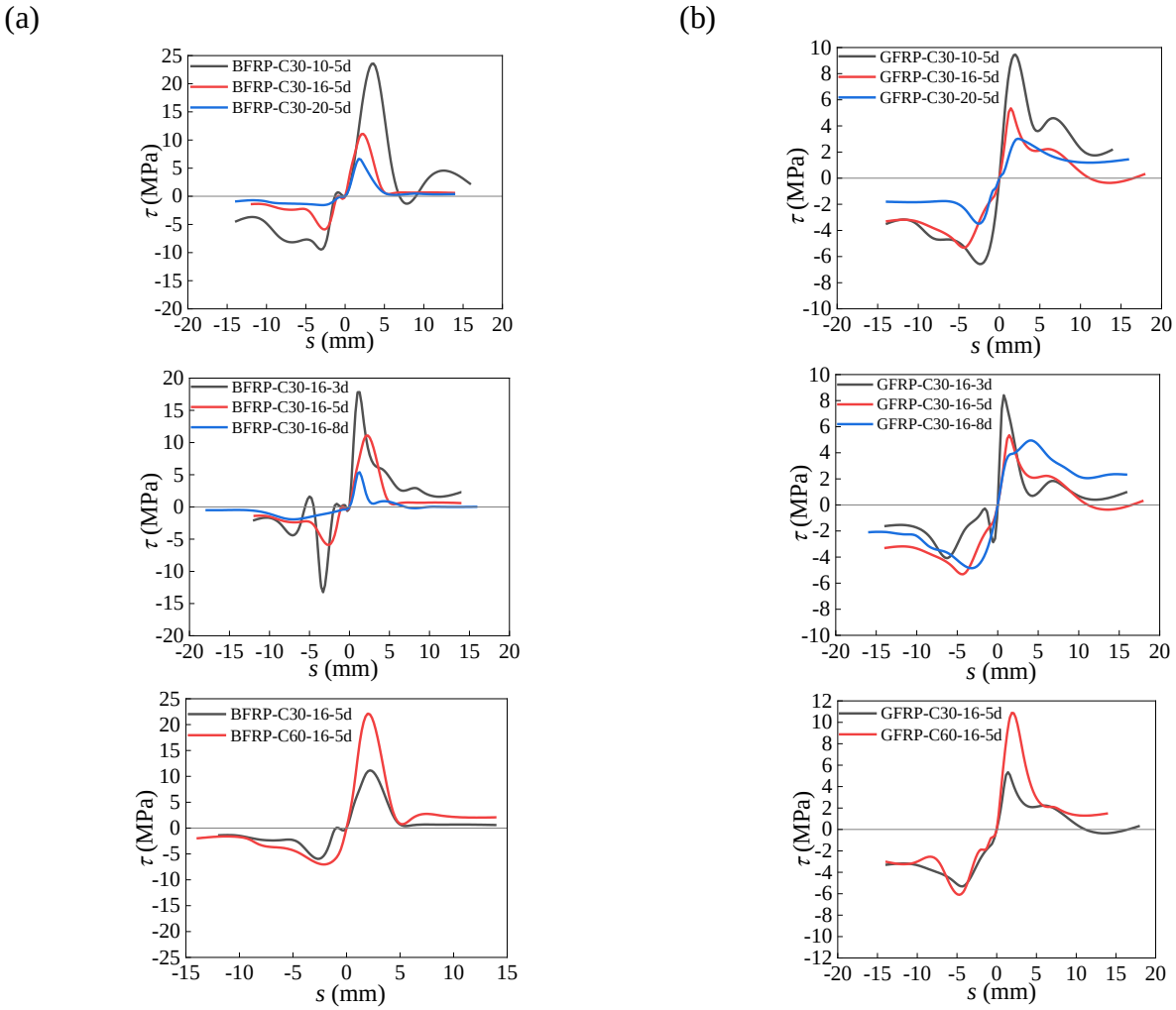

Figure 6. Bond stress-slip curve. **(a)** BFRP bars; **(b)** GFRP bars.

Table 4 gathers all characteristic values of $\tau - s$ curves for BFRP, CFRP and GFRP bars embedded in concrete subjected to reversed cyclic loading. Here, τ^+ and τ^- denote the maximum bond stress in the positive and negative directions, s^+ and s^- denote the slip corresponding to τ^+ and τ^-, with subscript u, r, e the ultimate, residual and elastic stress and slip, respectively.

Table 4. Test results (mean ± standard deviation, n = 5).

Specimen	τ_e^+ (MPa)	τ_e^- (MPa)	s_e^+ (mm)	s_e^- (mm)	τ_u^+ (MPa)	τ_u^- (MPa)	s_u^+ (mm)	s_u^- (mm)	τ_r^+ (MPa)	τ_r^- (MPa)	s_r^+ (mm)	s_r^- (mm)
BFRP-C30-10-5d	6.35 ± 0.07	–50 ± 0.15	1.18 ± 0.02	–1.41 ± 0.04	23.10 ± 0.80	–8.22 ± 0.40	3.85 ± 0.59	–8.35 ± 0.36	6.11 ± 0.02	–4.53 ± 0.25	5.83 ± 0.43	–6.08 ± 0.20
BFRP-C30-16-5d	4.17 ± 0.13	–0.21 ± 0.27	0.63 ± 0.03	–1.09 ± 0.24	10.53 ± 0.71	–3.15 ± 0.37	1.83 ± 0.04	–1.60 ± 0.56	1.56 ± 0.19	–1.44 ± 0.27	4.89 ± 0.50	–6.02 ± 0.11
BFRP-C30-20-5d	2.10 ± 0.21	–0.09 ± 0.34	0.69 ± 0.13	–0.57 ± 0.07	6.66 ± 0.76	–1.50 ± 0.71	1.75 ± 0.38	–3.67 ± 0.74	0.48 ± 0.23	–0.87 ± 0.32	8.98 ± 0.52	–9.15 ± 0.13
BFRP-C30-16-3d	2.45 ± 0.33	–0.87 ± 0.80	0.51 ± 0.48	–0.51 ± 0.88	17.82 ± 0.98	–12.43 ± 0.64	1.03 ± 1.02	–3.53 ± 0.73	2.86 ± 0.25	–2.84 ± 0.42	6.30 ± 0.42	–6.17 ± 0.75
BFRP-C30-16-8d	2.13 ± 0.52	–0.40 ± 0.44	0.52 ± 0.41	–0.78 ± 0.60	5.38 ± 0.60	–1.89 ± 0.55	1.28 ± 0.36	–7.58 ± 0.71	0.58 ± 0.29	–0.28 ± 0.45	5.55 ± 0.39	–8.38 ± 1.12
BFRP-C60-16-5d	7.47 ± 0.11	–4 ± 0.47	0.67 ± 0.15	–0.51 ± 0.16	23.63 ± 0.56	–6.04 ± 0.58	2.02 ± 0.25	–2.08 ± 0.60	2.45 ± 0.32	–2.26 ± 0.56	8.71 ± 0.28	–9 ± 0.95
CFRP-C30-10-5d	2.82 ± 0.60	–2.42 ± 0.58	0.51 ± 0.52	–0.78 ± 0.19	12.60 ± 0.03	–11.23 ± 0.05	1.34 ± 0.35	–1.54 ± 0.38	5.84 ± 0.36	–4.58 ± 0.52	8 ± 0.25	–10 ± 0.87
CFRP-C30-16-5d	2.09 ± 0.67	–1.87 ± 0.64	1.03 ± 0.16	–0.51 ± 0.11	8.93 ± 0.44	–3.46 ± 0.84	2.06 ± 0.45	–4.06 ± 0.20	0.80 ± 0.54	–1.88 ± 0.92	6.06 ± 0.03	–6.69 ± 0.62
CFRP-C30-20-5d	1.63 ± 0.17	–1.06 ± 0.55	0.55 ± 0.82	–0.21 ± 0.16	6.61 ± 0.04	–2.86 ± 0.80	1.87 ± 0.86	–6.61 ± 0.31	1.15 ± 0.52	–1.05 ± 0.25	8.04 ± 0.19	–9.72 ± 1.23
CFRP-C30-16-3d	2.77 ± 0.22	–2.71 ± 0.72	0.51 ± 0.50	–0.33 ± 0.75	11.06 ± 0.22	–5.71 ± 0.73	2.59 ± 0.75	–4.11 ± 0.52	2.08 ± 0.48	–2.06 ± 0.24	8.79 ± 0.15	–11.05 ± 0.63
CFRP-C30-16-8d	3.21 ± 0.94	–2.65 ± 0.58	0.51 ± 0.82	–1.03 ± 0.18	5.90 ± 0.15	–2.82 ± 0.65	2.13 ± 0.69	–6.17 ± 0.63	2.07 ± 0.49	–2.38 ± 1.02	8.08 ± 0.79	–9.40 ± 0.95
CFRP-C60-16-5d	3.01 ± 0.87	–2.70 ± 0.65	0.51 ± 0.75	–0.76 ± 0.04	18.75 ± 0.12	–11.24 ± 0.32	3.69 ± 0.38	–2.30 ± 0.71	3.10 ± 0.50	–4.04 ± 0.95	4.13 ± 0.78	–6.18 ± 0.87
GFRP-C30-10-5d	2.63 ± 0.18	–1.43ν0.07	0.83 ± 0.98	–0.60 ± 0.65	9.46 ± 0.97	–6.44 ± 0.24	1.97 ± 0.47	–1.91 ± 0.25	2.20 ± 0.90	–3.52 ± 1.06	5.98 ± 0.58	–6.18 ± 0.79
GFRP-C30-16-5d	2.57 ± 0.41	–1.27 ± 0.74	1.18 ± 0.26	–0.53 ± 0.26	5.03 ± 0.24	–4.30 ± 0.52	1.18 ± 0.57	–4.21 ± 0.75	2.13 ± 0.90	–3.31 ± 0.32	4.02 ± 0.64	–4.21 ± 1.08
GFRP-C30-20-5d	1.43 ± 0.65	–0.69 ± 0.28	1.05 ± 0.39	–0.40 ± 0.60	2.98 ± 0.24	–2.58 ± 0.35	2.61 ± 0.63	–1.56 ± 0.69	2.98 ± 0.31	–1.80 ± 0.25	6.06 ± 0.39	–3.98 ± 1.10
GFRP-C30-16-3d	3.40 ± 0.78	–2.63 ± 0.11	0.49 ± 0.62	–0.28 ± 0.42	7.96 ± 0.23	–4.07 ± 0.47	1.03 ± 0.25	–6.16 ± 0.52	1.80 ± 0.32	–1.69 ± 0.36	1.03 ± 0.76	–6.16 ± 0.56
GFRP-C30-16-8d	3.39 ± 0.32	–3.67 ± 0.27	1.04 ± 0.93	–0.62 ± 0.11	4.45 ± 0.79	–3.67 ± 0.36	3.99 ± 0.64	–6.20 ± 0.46	2.32 ± 0.36	–2.10 ± 0.39	3.99 ± 0.85	–6.20 ± 0.87
GFRP-C60-16-5d	2.67 ± 0.23	–1.74 ± 0.61	0.55 ± 0.72	–0.72 ± 0.88	10.67 ± 0.63	–5.66 ± 0.48	1.67 ± 0.35	–4.06 ± 0.38	1.80 ± 0.42	–3.18 ± 0.78	8.04 ± 0.89	–9.97 ± 1.02

3.3. Analysis of the bond stress-slip properties of different FRP bars

For different types of FRP-reinforced concrete, various factors exert varying levels of influence on their bond stress-slip characteristics. The impact of bar diameter, embedment length, and concrete strength on key bond performance indicators—such as maximum bond stress (the peak stress in the bond stress-slip curve), bond stiffness (the initial slope of the bond stress-slip curve), bond strength (the stress at which bond failure occurs), frictional bond resistance, and accumulated energy dissipation—was investigated. These performance indicators will be discussed in detail below.

3.3.1. Comparison of maximum bond stress of different types of FRP bars

The interfacial bond performance of FRP bars exhibits material-dependent characteristics governed by their mechanical properties and geometric features. BFRP bars demonstrate superior peak bond stress compared to CFRP and GFRP counterparts, attributed to enhanced mechanical interlock and frictional resistance arising from their pronounced surface ribs [52]. In contrast, CFRP and GFRP bars with less defined rib geometries exhibit reduced interfacial engagement, resulting in lower peak stresses. This disparity persists across parametric variations in diameter, embedment length, and concrete strength (Figure 7(a)–(c)).

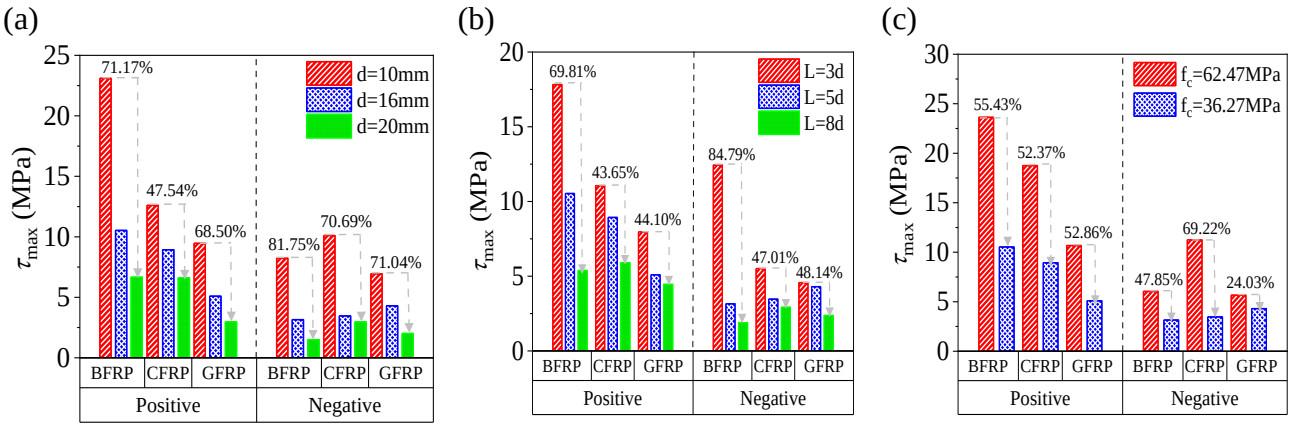

Figure 7. The peak bond stress. **(a)** Diameter; **(b)** Embedment length; **(c)** Concrete compressive strength.

For diameter effects (Figure 7(a)), increased bar dimensions marginally reduce peak bond stress across all FRP types, though CFRP bars show the least sensitivity due to their high strength and limited deformation capacity under stress [53–54]. The inherent stiffness of CFRP minimizes diameter-induced stress redistribution, maintaining interfacial stability even at larger scales. Similarly, embedment length variations (Figure 7(b)) exert negligible influence on CFRP bond stress, as their high strength prevents localized shear concentrations and maintains uniform stress distribution along the bond interface [55]. Conversely, in comparison to CFRP, BFRP and GFRP systems exhibit greater parametric sensitivity, attributable to their lower elastic moduli and more compliant behavior, despite maintaining an overall linear elastic response.

Concrete strength variations (Figure 7(c)) further highlight this material dichotomy: CFRP bars effectively buffer stress perturbations through their high intrinsic strength, while BFRP/GFRP systems

experience amplified bond stress variations because of their lower stiffness and greater strain under load, within the elastic range. These observations collectively underscore that CFRP's high stiffness and strength stabilize interfacial behavior against geometric and material parameter changes, whereas the relatively lower stiffness of BFRP and GFRP bars increases their sensitivity to parametric variations, even though all systems remain primarily linear elastic.

3.3.2. Stiffness degradation

The stiffness degradation coefficient κ, defined as $\kappa = \frac{K_n}{K_0}$, where K_{n} represents the unloading stiffness at each unloading cycle and K_0 denotes the initial unloading stiffness. Quantifying the reduction in unloading stiffness during cyclic loading, is influenced by multiple interfacial parameters as shown in Figure 8(a)–(b). For specimens with larger-diameter FRP bars, the enhanced contact area promotes stress homogenization through two complementary mechanisms: (1) stress dispersion across micro-regions, mitigating localized peaks, and (2) defect averaging that statistically reduces the impact of interfacial imperfections, analogous to composite size effects [56]. These mechanisms synergistically slow material wear, yielding higher κ values despite the theoretical increase in defect probability, particularly evident in FRP-concrete systems where concrete heterogeneity necessitates larger bond areas for stress redistribution. Similarly, extended embedment lengths enhance bond performance by enabling progressive stress transfer along the interface, delaying localized damage accumulation [57–58]. Concrete strength further modulates κ, with high-strength concrete exhibiting slower stiffness degradation due to superior compressive resistance and interfacial integrity [57]. Material-specific behaviors are pronounced in CFRP bars, where high stiffness and strength result in elevated initial κ and gradual degradation, contrasting with BFRP and GFRP systems that exhibit accelerated κ reduction due to lower modulus and interfacial roughness [59–61]. These collective observations underscore the interdependence of geometric, material, and interfacial factors in governing stiffness degradation dynamics.

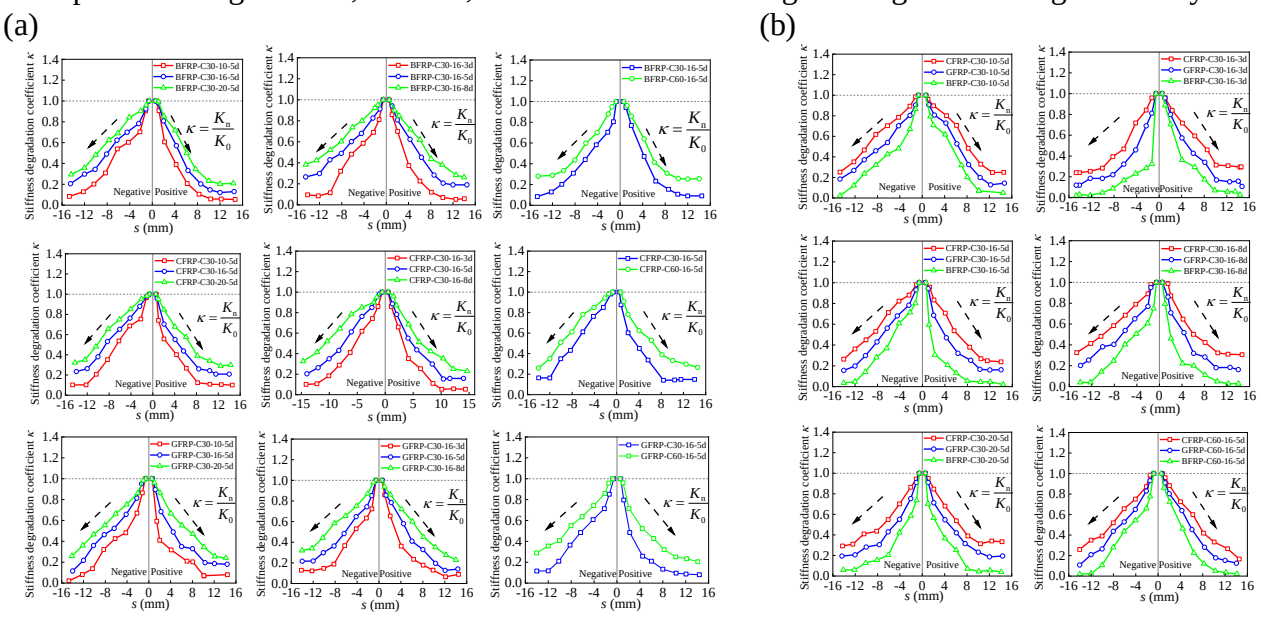

Figure 8. Stiffness degradation coefficient. **(a)** Different working conditions; **(b)** Comparison of different FRP bars.

3.3.3. Strength degradation

The strength degradation coefficient η, defined as $\eta = \frac{\tau_n}{\tau_u}$, where τ_n is the peak bond stress recorded at the onset of each unloading phase during cyclic loading and τ_u is the maximum bond strength attained over the entire loading process [62], quantifies the reduction in bond capacity during cyclic unloading and provides critical insights into interfacial deterioration mechanisms (Figure 9(a)). Before reaching the peak bond stress (τ_u), η increases gradually with slip, indicating progressive damage accumulation at the FRP-concrete interface. Upon reaching τ_u, typically associated with the initiation of concrete cracking, bond degradation accelerates sharply, leading to a rapid drop in η toward a residual plateau, thereby establishing τ_u as a key marker of interfacial failure [62–63]. Parametric analyses reveal that larger-diameter bars retain higher η values due to their increased contact area, which promotes uniform stress distribution and mitigates localized damage [54]. Similarly, extended embedment lengths enhance interfacial friction and mechanical interlocking [57], sustaining bond integrity and slowing the decay of η through progressive stress redistribution. High-strength concrete further stabilizes η by improving micro-mechanical interlock and surface wear resistance [64], whereas low-strength concrete systems exhibit more rapid degradation. Among different FRP types, CFRP bars display superior η performance (Figure 9(b)) compared to BFRP and GFRP bars, attributed to their higher elastic modulus, which restricts interfacial slip and limits damage propagation. These findings collectively underscore that strength degradation is primarily governed by the capacity for stress redistribution rather than by the likelihood of initial defects, especially in heterogeneous FRP-concrete systems where geometric and material factors interact nonlinearly to control interfacial behavior.

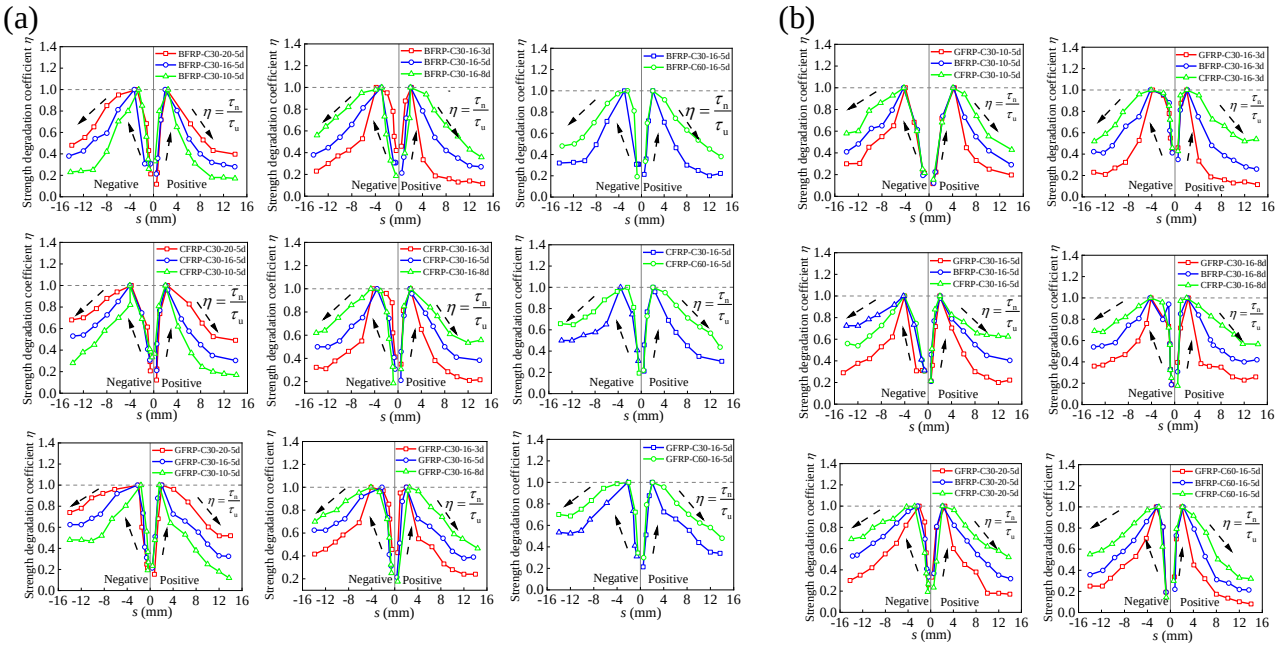

Figure 9. Strength degradation coefficient. **(a)** Different working conditions; **(b)** Comparison of different FRP bars.

3.3.4. Frictional degradation

Frictional degradation, quantified by the coefficient $\lambda = \frac{F_n}{F_0}$ (where F_n is the cyclic frictional resistance and F_0 the initial value), critically governs the post-peak bond behavior and long-term durability of FRP-concrete interfaces [55,59,65]. As shown in Figure 10(a), λ exhibits a triphasic evolution: initial stability during elastic loading, progressive decline post-peak, and eventual stabilization at a residual plateau dominated by interfacial friction. Larger-diameter bars reduce unit-area stresses through enhanced contact area, mitigating wear rates and preserving λ [66]. Extended embedment lengths promote stress homogenization along the interface, delaying localized damage accumulation [65]. High-strength concrete resists micro-cracking and interfacial wear, maintaining higher λ values compared to low-strength counterparts. CFRP bars exhibit superior friction retention due to their high modulus limiting interfacial deformation, followed by BFRP and GFRP, where smoother surfaces and lower stiffness accelerate degradation (Figure 10(b)) [59]. The interdependence of these factors underscores that frictional degradation arises from competing mechanisms: while larger interfacial areas statistically increase defect probability, stress redistribution capabilities dominate under typical service conditions, particularly in heterogeneous systems like FRP-concrete composites.

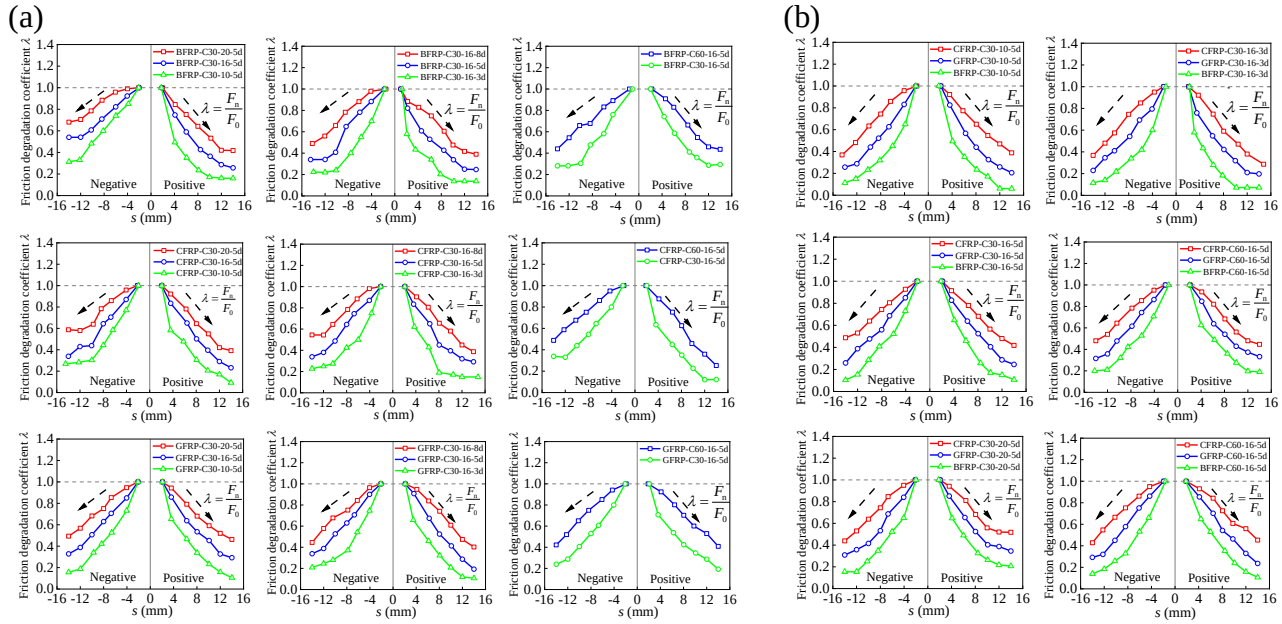

Figure 10. Frictional degradation coefficient. **(a)** Different working conditions; **(b)** Comparison of different FRP bars.

3.3.5. Cumulative energy dissipation

The cumulative energy dissipation (E_{total}) for each specimen was quantified by integrating the areas enclosed within individual hysteresis loops [63]. Figure 11 illustrates the influence of FRP bar diameter, embedment length, and concrete strength on E_{total} As depicted in Figure 11(a), specimens reinforced with larger-diameter bars demonstrate significantly higher E_{total} compared to those with smaller diameters. This observation suggests that, under identical FRP bar configurations and cycle counts, larger-diameter bars exhibit enhanced energy absorption and dissipation capabilities during cyclic loading. The increased interfacial contact area and improved stress distribution associated with larger

diameters facilitate greater energy dissipation during slip progression, thereby contributing to the observed elevation in E_{total}.

In addition, the cumulative energy dissipation of long embedding lengths is greater than that of short embedding lengths, as shown in Figure 11(b). Shorter embedding lengths provide insufficient bonding and friction, which can lead to larger slip displacements during cyclic loading [55]. This often results in premature bond failure and consequently lower cumulative dissipated energy. Concrete strength also plays a significant role in the cumulative energy dissipation of the specimens [60], as demonstrated in Figure 11(c). Low-strength concrete tends to slip and crack at the interface more readily, leading to premature bond failure. Although some energy is absorbed during the slip process, the overall cumulative dissipated energy remains low.

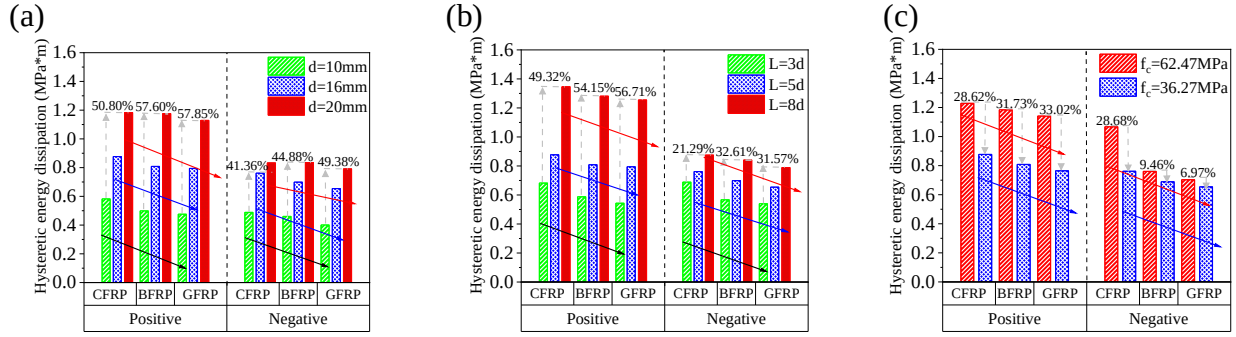

Figure 11. Energy dissipation. **(a)** Diameter; **(b)** Embedment length; **(c)** Concrete compressive strength.

As shown in Figure 11, the cumulative energy dissipation of CFRP-reinforced specimens was significantly higher than that of BFRP- and GFRP-reinforced specimens throughout the loading cycles. This superior performance can be attributed to the higher tensile strength and better bond characteristics of CFRP bars, which enable greater resistance against interfacial degradation and sustained energy absorption under cyclic loading. Consequently, CFRP bars demonstrate a more favorable hysteretic response, with greater cumulative energy dissipation, implying enhanced ductility and toughness essential for seismic applications.

Based on these observations, CFRP-reinforced concrete exhibits superior suitability for seismic design compared to BFRP- and GFRP-reinforced systems. The higher energy dissipation capacity of CFRP enhances the overall seismic resilience by enabling structures to undergo larger deformations while maintaining load-carrying capacity. In contrast, the relatively brittle behavior and lower energy dissipation observed in BFRP- and GFRP-reinforced specimens suggest that these materials may require additional design considerations, such as increased confinement or hybrid reinforcement strategies, to ensure adequate performance in high seismicity regions.

3.3.6. Influence of material properties on the bond behavior of BFRP, CFRP, and GFRP bars

The bond performance of FRP bars in concrete exhibits significant material-specific variations due to differences in fiber composition, surface characteristics, and interfacial mechanics among BFRP, CFRP, and GFRP systems. BFRP bars, composed of basalt fibers, demonstrate intermediate stiffness and tensile strength compared to CFRP and GFRP bars; however, their bond behavior is notably influenced by the natural roughness of the basalt fibers and the geometry of the ribs, which are

optimized for mechanical interlock. Studies by Shen *et al.* [38] reveal that BFRP bars with tightly spaced ribs (e.g., 12 mm spacing and 2.5 mm width) achieve superior bond strength due to enhanced stress distribution along the interface, although excessive rib height may induce premature concrete splitting in high-strength matrices. CFRP bars, characterized by their high stiffness and smooth carbon fiber surfaces, rely heavily on surface treatments such as sand coating or helical winding to improve bond capacity. The reduced surface friction of CFRP bars necessitates aggressive rib geometries to compensate for lower adhesion, often resulting in higher initial bond stiffness but accelerated degradation under cyclic loading due to localized stress concentrations at the rib edges [39,45].

In contrast, GFRP bars, with their lower modulus and higher ductility, exhibit bond behavior dominated by resin-matrix interactions. The susceptibility of the glass fibers to moisture ingress and alkaline environments necessitates specialized surface coatings (e.g., epoxy-based treatments) to mitigate interfacial degradation. Lee *et al.* [43] observed that GFRP bars with wider rib spacing exhibit progressive bond failure, as the resin-rich surface allows gradual stress redistribution, whereas bars with narrower rib spacing concentrate stresses, leading to abrupt pull-out failures. Notably, the deformation coefficient (rib width-to-spacing ratio) plays a critical role in GFRP bond performance, with higher ratios shifting failure modes from pull-out to concrete splitting, particularly in ultra-high-performance concrete (UHPC) systems [45].

Material-specific mechanisms further differentiate bond degradation under cyclic loading. The high stiffness of CFRP bars exacerbates interfacial shear stress reversal, amplifying frictional wear at rib-concrete contact points, whereas the inherent roughness of BFRP fibers promotes residual frictional resistance even after partial debonding. In contrast, GFRP bars suffer from resin plasticity under repeated loading, leading to irreversible slip accumulation and reduced energy dissipation. Surface treatments such as sandblasting or hybrid rib configurations (e.g., square *versus* round ribs) further modulate these trends. For instance, Achillides *et al.* [20] demonstrated that square-ribbed CFRP bars achieve a 25% higher bond strength than round-ribbed counterparts due to enhanced wedging effects, whereas similar treatments in GFRP bars yield diminishing returns due to the brittleness of the resin matrix.

These distinctions underscore the necessity of adopting material-tailored design approaches. While the high performance of CFRP bars justifies their use in stiffness-critical applications, the balanced mechanical and interfacial properties of BFRP bars make them suitable for environments requiring corrosion resistance and moderate bond durability. GFRP bars, despite their cost-effectiveness, demand careful consideration of environmental exposure and rib geometry to ensure long-term bond integrity. Future research should prioritize quantifying the synergistic effects of rib geometry, surface treatment, and environmental exposure across different FRP types to refine predictive models and codify design guidelines for diverse structural applications.

4. Unified formula of bond stress-slip relationship

From the analysis of hysteresis curves discussed in Section 3.2, it is evident that the bond stress-slip behaviors of BFRP, GFRP, and CFRP bars exhibit notable similarities. The constitutive relationship for bond stress-slip that is valid for CFRP bars can also be adapted for BFRP and GFRP bars with some adjustments. Consequently, a hysteresis model for bond stress-slip has been developed to represent the hysteresis curves of FRP bars embedded in concrete. This model considers the material-specific characteristics of the FRP bars as well as the interaction at the FRP–concrete interface, which are critical

for accurately simulating the cyclic loading response. Figure 12 illustrates this model, which comprises two primary components: (1) the skeleton curve model and (2) the hysteresis law.

The skeleton curve model represents the envelope of the bond stress-slip curve, capturing the overall elastic and post-peak behavior of the FRP–concrete interface. It serves as the fundamental framework for understanding the maximum bond stress achieved during loading cycles. The skeleton curve is defined by a four-stage bond-slip relationship, characterized by: (i) an initial linear elastic ascending branch; (ii) a nonlinear hardening branch up to the peak bond stress (τ_u); (iii) a softening branch representing the degradation of bond strength with increasing slip; and (iv) a residual plateau where bond stress stabilizes at a residual value (τ_r) for large slip values. Key parameters include the initial stiffness, peak bond stress (τ_u), slip at peak (s_u), and residual bond stress (τ_r).

Conversely, the hysteresis law describes the energy dissipation and bond strength degradation during unloading and reloading phases. This part of the model is essential for simulating the cyclic behavior of the interface, reflecting the inelastic response and progressive damage accumulation over multiple loading cycles. Specifically, during unloading, the bond stress decreases linearly with slip reduction at a degraded unloading stiffness, which depends on the maximum slip previously attained. Upon reloading, a path with further reduced stiffness is followed until it rejoins the skeleton curve. The model incorporates two critical hysteresis features: (i) stiffness degradation as a function of maximum historical slip, and (ii) slip offset during load reversals, representing irreversible slip accumulation at the FRP-concrete interface.

Figure 12 schematically illustrates the four-stage skeleton curve and the corresponding unloading/reloading paths governed by the hysteresis law. Transitional points (such as the peak point, softening initiation point, and residual plateau onset) and key slopes (initial stiffness, unloading stiffness, and reloading stiffness) are clearly marked to facilitate understanding and implementation.

Together, these components provide a comprehensive framework for simulating the bond stress-slip behavior of FRP bars under cyclic loading, which is vital for understanding the long-term performance of FRP-reinforced concrete structures.

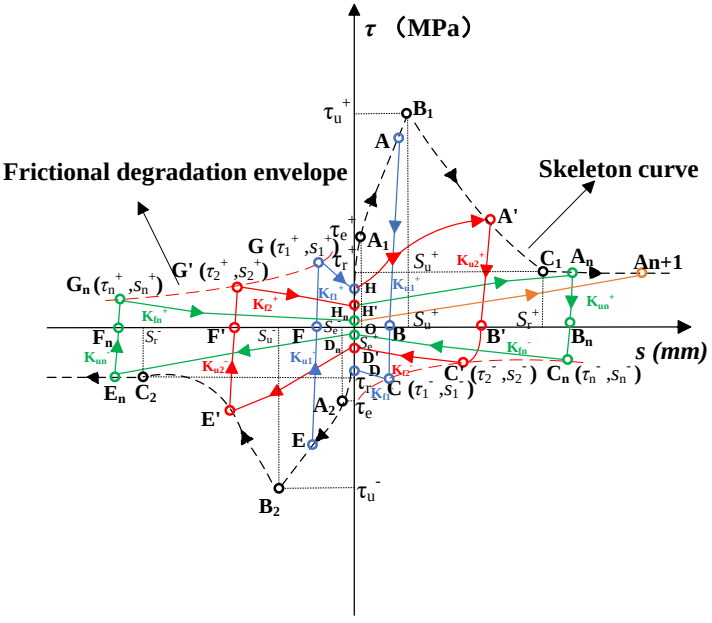

Figure 12. Bond stress-slip constitutive model.

4.1. Unified skeleton curve constitutive model considering various structural characteristics

By comparing the bond stress ratio [67] ($\varsigma = \frac{\tau_{B,G}}{\tau_C}$) between CFRP bars and BFRP bars, a correction factor can be derived, allowing the CFRP bond-slip constitutive model to be adapted for predicting the behavior of BFRP bars. Specifically, the bond stress ratio between CFRP and BFRP bars is first determined through experimental or theoretical analysis, which reflects the differences in the interfacial bonding performance of the two materials. This bond stress ratio is then used as a correction factor, multiplying the parameters related to bond strength in the CFRP model to obtain a modified model suitable for BFRP bars. Finally, the accuracy of the modified model in predicting the bond-slip behavior of BFRP bars in concrete is validated through experiments or numerical simulations. Similarly, this approach can be applied to GFRP bars [68–69]. This method, utilizing the bond stress ratio to derive a correction factor, provides an effective approach for transforming CFRP-based models into accurate models that describe the behavior of BFRP bars.

Taking the elastic stage as an illustrative case, the evolution of normalized bond stress parameters (ς_{e^+} and ς_{e^-}) for BFRP and GFRP bars is presented in Figure 13 as a function of embedment length, with variations in bar diameter and concrete strength explicitly considered. In this context, τ^+ and τ^- represent the maximum bond stresses in the positive and negative loading directions, respectively, while s^+ and s^- denote the corresponding slip values at these stress peaks. Subscripts B, C, and G are used to differentiate the bond stress and slip parameters for BFRP, CFRP, and GFRP bars, respectively. Building upon the authors' previous work [51], the bond stress-slip relationship for CFRP bars can be mathematically expressed as follows:

$$\tau_c^+ = 117.13\left(\frac{L}{d}\right)^{-0.22} d^{-2.03} f_c \beta \eta s \tag{2}$$

$$\tau_c^- = 82.73\left(\frac{L}{d}\right)^{-0.22} d^{-2.22} f_c \beta \eta s \tag{3}$$

Considering that BFRP, CFRP and GFRP all behave linear elastically but with different material parameters, the bond stress-slip relationship for BFRP and GFRP takes a similar form to CFRP:

$$\tau_{B,G}^+ = \varsigma_{e^+}\tau_C^+ \tag{4}$$

$$\tau_{B,G}^- = \varsigma_{e^-}\tau_C^- \tag{5}$$

For the BFRP bar, the correction coefficient ς_{e^+} and ς_{e^-} expressed as obtained by non-linear regression analysis with test data:

$$\varsigma_{e^+} = 7.92e^{-0.09d-0.02L} f_c^{0.50} \tag{6}$$

$$\varsigma_{e^-} = 9.56e^{-0.37d-0.02L} f_c^{0.50} \tag{7}$$

For the GFRP bar, with ς_{e^+} and ς_{e^-} expressed as follows:

$$\varsigma_{e^+} = 45.36e^{-0.15d-0.04L} f_c^{0.50} \tag{8}$$

$$\varsigma_{e^-} = 1.41e^{-0.15d-0.01L} f_c^{0.50} \tag{9}$$

The τ – s relationship across these four stages can be reduced to a unified form due to their similar mathematical expression. Despite the apparent differences in their conditions, it can be expressed by the following formulas:

$$\tau = \mathrm{A}d^{\mathrm{B}}\mu^{\mathrm{C}}f_c^{D}\beta^{\mathrm{E}}\eta s^{\mathrm{F}} - Gf_c\beta H \tag{10}$$

with $\mu = \frac{L}{d}$; $\beta = \frac{h}{d}$; $\eta = \frac{C_1}{C_2}$, and the subscripts + and – denoting the positive and negative cycles, respectively. Appendix B and C list the fitted values of parameters A, B, C, D, E, F, G and H involved in Equation (10) for the micro-slip, slip, degradation, and residual stage of the τ-s relationship.

(a)

(b)

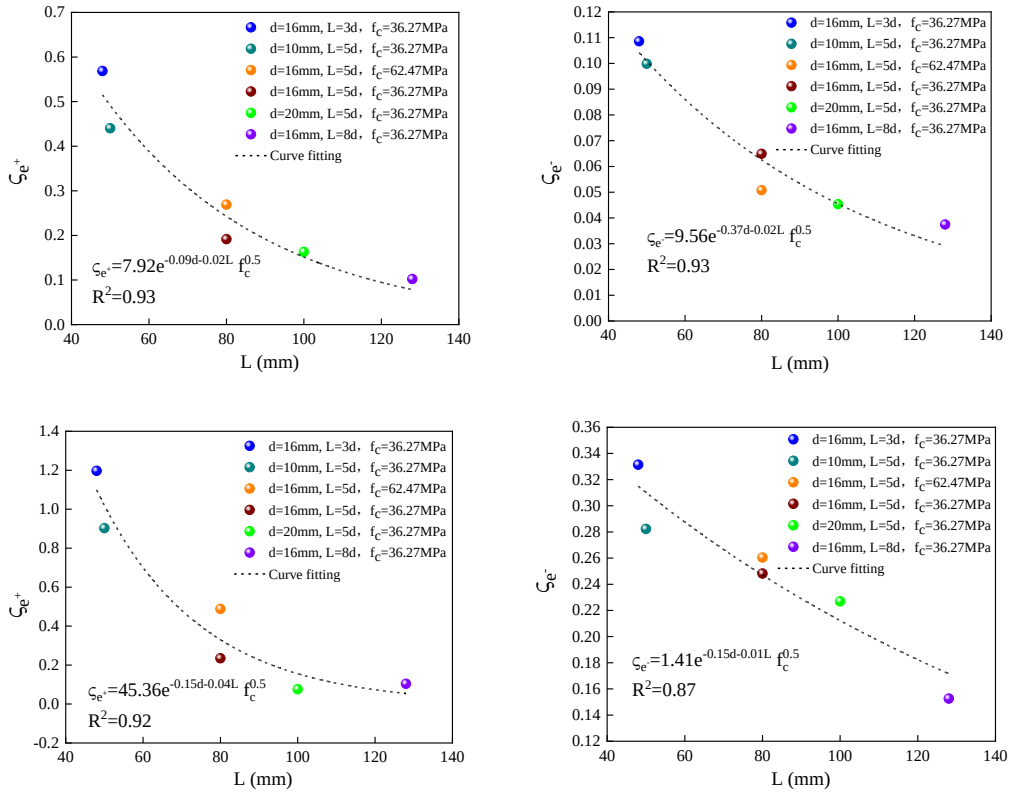

Figure 13. The relationship between the mirco-slip stage bond stress and the diameter of the FRP bars, embedment length and concrete compressive strength. **(a)** BFRP bars; **(b)** GFRP bars.

4.2. Hysteretic curve constitutive model

Since the hysteresis curve provides a clear depiction of the bond performance between FRP bars and concrete, by analyzing multiple cycles of the hysteresis curve, the degree of degradation of the bond strength can be observed [67], showing how the bond performance decays with the increase in the number of loading times. In addition, the enclosed area of the hysteresis curve represents the energy dissipated by the system in the loading and unloading cycles [70]. As the number of cycles applied to the load rises, the change in energy dissipation can reflect the damage accumulation of the interface. The shape and area changes of the hysteresis curve reflect the change in stiffness of the interface between FRP bars and concrete [71]. Therefore, it is also necessary to derive and study the hysteresis curve model.

4.2.1. The slopes K_u of AC and EG segment

The slopes of the segments AC and EG are denoted as K_u^+ and K_u^- in Figure 12. Figure 14(a) illustrates the correlation between K_u and the peak bond stress τ_{ui} for each cycle. Some researchers suggest that prior to reaching the maximum bond stress τ_u, the value of K_u remains relatively constant across different cycles [52]. However, once the maximum bond stress τ_u is exceeded, K_u tends to vary and exhibits a certain pattern, which has been elaborated upon in Section 3.3.2. The bond stress-slip curves of CFRP bars, GFRP bars and BFRP bars have certain similarities, and the stiffness degradation and friction degradation trends are the same. The data of these three bars can be fully fitted to obtain a unified formula for expressing K_u and the peak bond stress τ_{ui}. Even though Figure 14(a) appears nearly linear, the choice of a quadratic polynomial fit is intended to more accurately capture potential curvilinear effects, particularly in the higher stress range. Furthermore, a quadratic polynomial provides a more flexible fitting model for subsequent analysis, as it retains sufficient fitting capacity to accommodate potential variations, even if the data points appear linear in certain regions. On this basis, the calculation formulas for the slopes K_u in the positive and negative directions of the AC and EG segments were established.

$$\begin{cases} K_u^+ = 0.99 + 1.21\tau_{ui} + 0.003\tau_{ui}^2 \\ K_u^- = 3.19 + 0.95\tau_{ui} + 0.024\tau_{ui}^2 \end{cases} \tag{11}$$

(a)

(b)

(c)

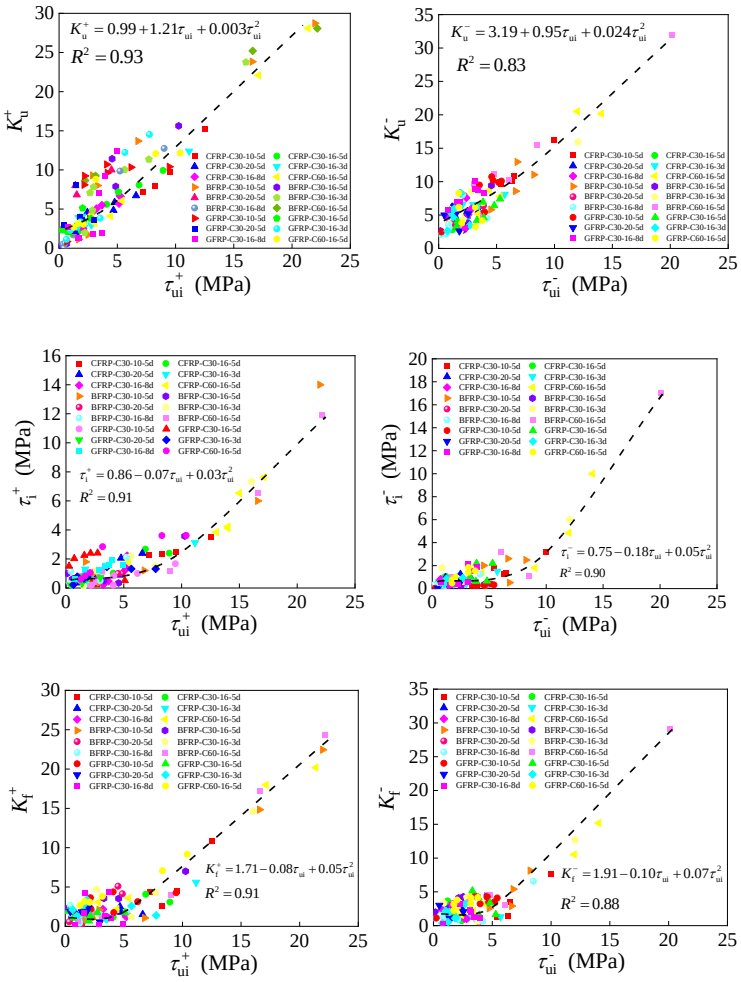

Figure 14. The relationship. **(a)** K_u and the τ_{ui}; **(b)** τ_i and τ_{ui}; **(c)** K_f and the τ_{ui}.

4.2.2. The slopes K_f of CD and GH segment

This section begins with points G (s_1^+, τ_1^+) and point C (s_1^-, τ_1^-) in both the positive and negative directions, as depicted in Figure 12. Figure 14(b) illustrates the correlation between the bond stress τ_{i} and the peak bond stress τ_{ui} for each cycle prior to reaching the maximum bond stress. For specimens with different diameters, different embedment lengths and different concrete strengths, the τ_{i} value has a nonlinear relationship with τ_{ui}. The nonlinear correlation between the values of τ_{i} and τ_{ui} are established as follows:

$$\begin{cases} \tau_i^+ = 0.86 - 0.07\tau_{ui} + 0.03\tau_{ui}^2 \\ \tau_i^- = 0.75 - 0.18\tau_{ui} + 0.05\tau_{ui}^2 \end{cases} \tag{12}$$

The slip s_i of the CD and GH segments can be determined using the following formula:

$$\tau_{ui} - \tau_i = K_u(s_{ui} - s_i) \tag{13}$$

The slopes of the CD segment and the GH segment are denoted as K_f^+ and K_f^-, respectively. Figure 14(c) shows the relationship between K_f and τ_{ui}. The nonlinear relationship between K_f and τ_{ui} are established as follows:

$$\begin{cases} K_f^+ = 1.71 - 0.08\tau_{ui} + 0.05\tau_{ui}^2 \\ K_f^- = 1.91 - 0.10\tau_{ui} + 0.07\tau_{ui}^2 \end{cases} \tag{14}$$

4.2.3. Model validation

To validate the proposed models, the predicted curves were compared with experimental results and existing datasets from Shen *et al.* [53], Zhao *et al.* [52], Gong *et al.* [39], and J. Y. Lee *et al.* [43], which remain among the limited comprehensive studies on the cyclic bond behavior of FRP bars in concrete. Figure 15(a) and Figure 15(b) demonstrate the agreement between the proposed models and experimental data across various FRP bar specimens, showing reasonable alignment despite minor discrepancies in high bond stress regimes. While the model performs well under controlled laboratory conditions, its generalizability requires further validation through broader experimental datasets and real-world structural applications. Future efforts will focus on incorporating environmental effects and long-term loading scenarios to enhance practical relevance.

The asymmetry evident in Figure 15, particularly in the skeleton and hysteresis models, stems from the inherent directional dependency of FRP-concrete interfacial mechanics under cyclic loading. This phenomenon arises from the anisotropic nature of FRP materials, where tensile loading engages fiber-dominated resistance through enhanced fiber-matrix synergy, while compressive loading triggers matrix-dominated failure mechanisms such as localized crushing. In the skeleton model (Figure 15(a)), the lower bond stress intercept in the negative direction reflects reduced frictional recovery under compression, a consequence of irreversible matrix damage and incomplete crack closure during load reversal. Post-test microstructural analyses corroborate this behavior, revealing distinct damage patterns: fiber debonding in tension and matrix fragmentation in compression [21,38]. The hysteresis model (Figure 15(b)) further highlights accelerated stiffness degradation in the negative direction, driven by cumulative shear-induced microcrack coalescence under compressive stresses. Bidirectional loading exacerbates this asymmetry by inducing shear stress reversal and residual slip, which disproportionately redistributes interfacial stresses in FRP systems due to their low transverse

stiffness, allowing larger slip displacements under compression [43,52]. These observations align with experimental findings by Zhao *et al.* [52], who documented faster bond degradation in GFRP-concrete systems under compressive cycles.

From an engineering perspective, the observed asymmetry necessitates direction-specific adjustments in bond-slip models for seismic design. The reduced bond capacity in compression implies that FRP-reinforced compression zones may require enhanced confinement or surface treatments to prevent premature failure. Moreover, the divergent stiffness degradation trends between tensile and compressive paths demand separate consideration in constitutive models to accurately predict energy dissipation and residual strength. While the proposed model captures these directional effects with reasonable fidelity, discrepancies in high bond stress regimes suggest unaccounted mesoscale interactions, such as fiber-matrix interphase plasticity or environmental aging effects. Addressing these limitations will refine the model's predictive capability and broaden its applicability.

(a)

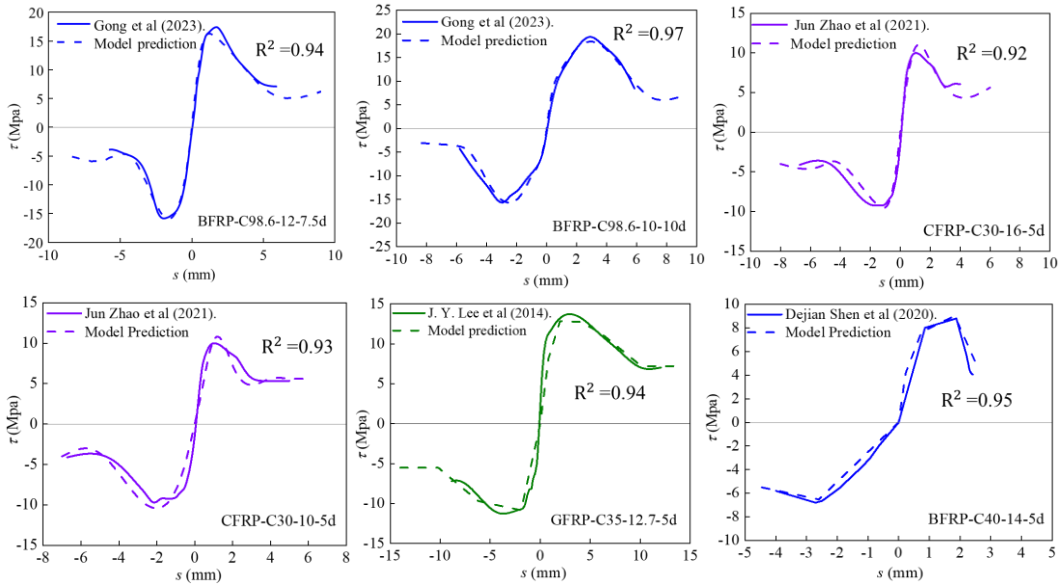

(b)

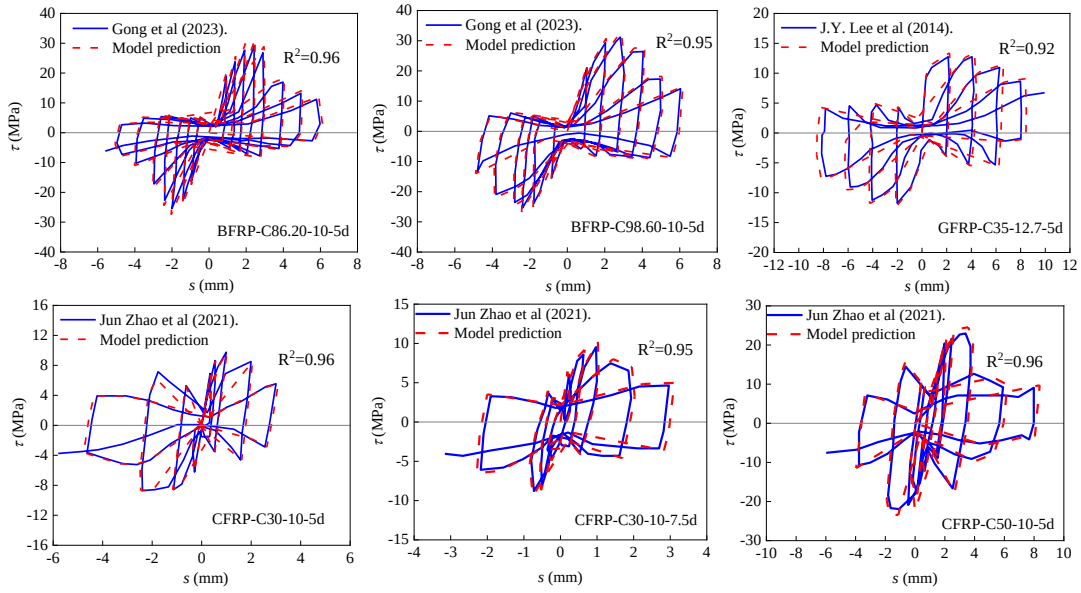

Figure 15. Comparison of the model proposed with existing experiments. **(a)** Skeleton model; **(b)** Hysteresis model.

In summary, the asymmetry in Figure 15 encapsulates the complex interplay of material anisotropy, cyclic damage accumulation, and interfacial stress redistribution. Bridging these directional dependencies within predictive models is essential for advancing the seismic resilience of FRP-reinforced structures, ensuring that theoretical advancements translate effectively into engineering practice.

5. Conclusion

This paper provides a comprehensive analysis of how concrete compressive strength, bar diameter, and embedment length impact the bonding performance of FRP bars. Based on the test results, a bond stress-slip model has been developed. This model offers a unified approach for predicting the bonding performance of BFRP, CFRP, and GFRP bars within concrete. The main conclusions are as follows:

(1) The bond stress of FRP bars is observed to decrease as the diameter or embedment length increases, while it increases with higher concrete strength. Notably, BFRP bars exhibit the highest bond stress among the different types.

(2) Compared with large diameter bars or long embedment length bars, the stiffness degradation, friction degradation and strength degradation of small diameter bars or short embedment length bars are relatively rapid; the stiffness degradation, friction degradation and strength degradation of specimens with high concrete strength are relatively slow.

(3) Specimens of FRP bars with increased diameters, extended embedment lengths, and higher concrete strengths show enhanced cumulative energy dissipation. Of these, CFRP bars exhibit the most effective energy dissipation compared to BFRP and GFRP bars.

(4) A comprehensive hysteresis model for bond-slip behavior was developed. This model effectively calculates the bond stress-slip relationships for three types of FRP bars subjected to cyclic loading and accurately describes how various parameters, such as concrete compressive strength, bar diameter, embedment length, rib height, rib width-to-width ratio, and rib spacing, influence the bond stress-slip performance.

Acknowledgments

This research work was financially supported by the National Natural Science Foundation of China (No. 52208453), and the Natural Science Foundation of Chongqing, China (CSTB2023NSCQ-MSX0682), and the Beijing Nova Program (20220484047). All support is gratefully acknowledged.

Authors' contribution

Bo Li: methodology, software, validation, formal analysis, investigation, writing—original draft preparation. Dong Li: supervision, funding acquisition, project administration. Fengjuan Chen: project administration, writing—review & editing, funding acquisition, resources. Liu Jin: project administration, resources, methodology. Xiuli Du: project administration, resources, methodology. All authors have read and agreed to the published version of the manuscript.

Conflicts of interests

The authors declare no conflict of interest.

Appendix

Appendix A. The Hysteretic curve

(a)

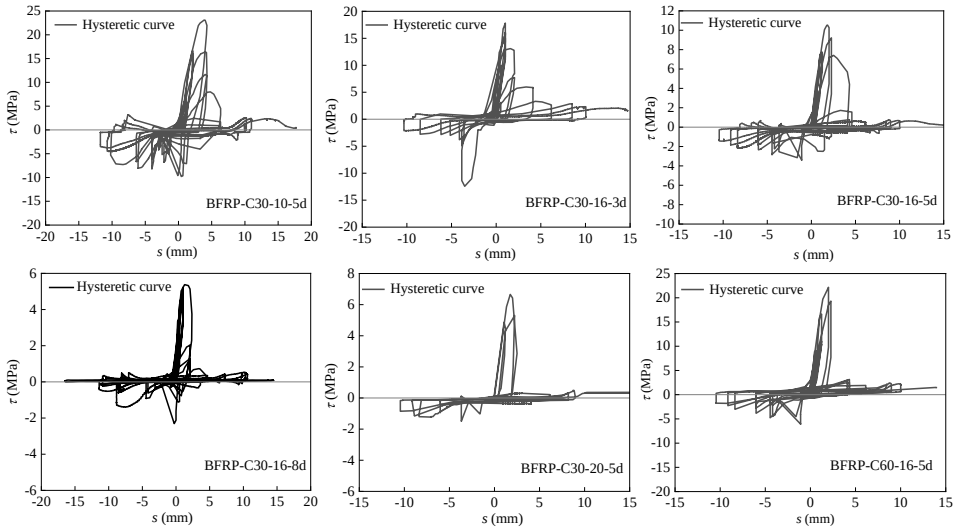

(b)

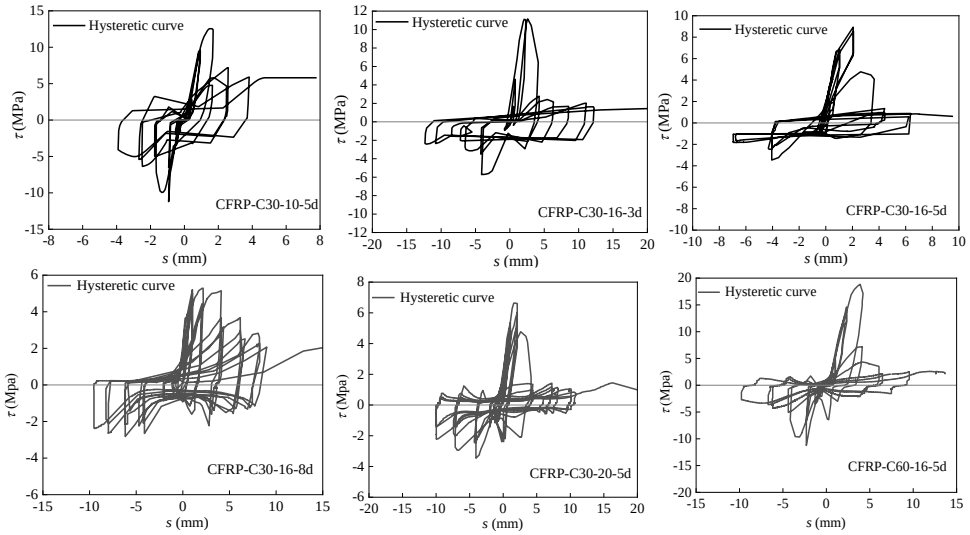

(c)

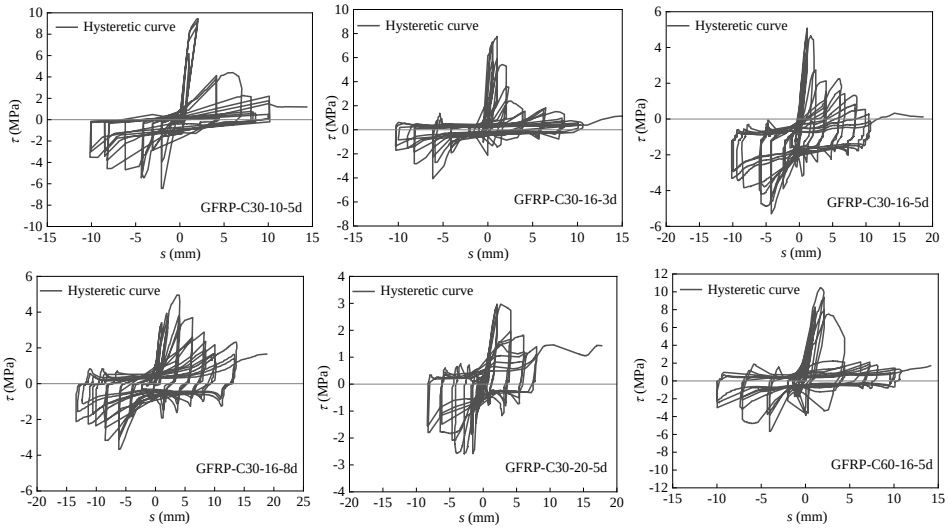

Figure A1. Hysteretic curve. **(a)** BFRP bars; **(b)** CFRP bars; **(c)** GFRP bars.

Appendix B. The fitting parameters in the formula (the positive cycle)

Table B1. Determination of K for the degradation stage.

$\mathbf{K = \gamma \cdot \varphi}$		$\boldsymbol{\lambda}$
γ	$\frac{a-b}{c-e}$	$\frac{l\kappa}{d}$
φ	$s - ef_c^{-0.50}\beta^{-0.50}(-0.94\lambda^2 + 1.40\lambda - 0.21)$	
a	$90.29d^{-0.98}\mu^{-0.92}(-1.36\lambda^2 + 2.15\lambda + 2.06)\varsigma_{u^+}$	
b	$74.98d^{-0.88}\mu^{-1.38}(-0.36\lambda^2 + 0.49\lambda + 0.51)\varsigma_{r^+}$	
c	$4.89d^{0.49}\mu^{-0.23}(-0.78\lambda^2 + 1.16\lambda - 0.10)$	
e	$2.60d^{0.53}\mu^{-0.27}(-0.94\lambda^2 + 1.40\lambda - 0.21)$	

Table B2. Determination of η for the 4 stages.

	$\boldsymbol{\eta}$	$\boldsymbol{\lambda}$
Micro-slip stage	$\frac{-4.39\lambda^2 + 6.64\lambda + 0.44}{0.52\lambda^2 - 0.76\lambda + 0.49}$	$\frac{l\kappa}{d}$
Slip stage	$\frac{-1.36\lambda^2 + 2.15\lambda + 2.06}{(-0.94\lambda^2 + 1.40\lambda - 0.21)^{0.32}}$	
Degradation stage	$-1.36\lambda^2 + 2.15\lambda + 2.06$	
Residual stage	$-0.36\lambda^2 + 0.49\lambda + 0.51$	

Note: $\beta = \frac{h}{d}$

In the above table, h, κ and l denote the rib heights, rib width-to-spacing ratios, rib spacings, respectively.

Appendix C. The fitting parameters in the formula (the negative cycle)

Table C1. Determination of K for the degradation stage.

$\boldsymbol{K = \gamma \cdot \varphi}$		$\boldsymbol{\lambda}$
γ	$\frac{a-b}{c-e}$	$\frac{l\kappa}{d}$
φ	$s - ef_c^{-0.50}\beta^{-0.50}(-0.60\lambda^2 + 0.94\lambda - 0.20)$	
a	$-62.31d^{-0.95}\mu^{-0.79}(-6.80\lambda^2 + 10.20\lambda - 0.78)\varsigma_{u^-}$	
b	$-119.03d^{-1.08}\mu^{-1.36}(-1.03\lambda^2 + 1.52\lambda - 0.20)\varsigma_{r^-}$	
c	$-4.14d^{0.68}\mu^{-0.34}(-0.71\lambda^2 + 1.04\lambda - 0.18)$	
e	$-10.20d^{0.51}\mu^{-0.97}(-0.60\lambda^2 + 0.94\lambda - 0.20)$	

Table C2. Determination of η for the 4 stages.

	$\boldsymbol{\eta}$	$\boldsymbol{\lambda}$
Micro-slip stage	$\frac{-5.66\lambda^2 + 8.40\lambda - 0.25}{-1.12\lambda^2 + 1.79\lambda - 0.45}$	$\frac{l\kappa}{d}$
Slip stage	$\frac{-6.80\lambda^2 + 10.20\lambda - 0.78}{(-0.60\lambda^2 + 0.94\lambda - 0.20)^{0.32}}$	
Degradation stage	$-6.80\lambda^2 + 10.20\lambda - 0.78$	
Residual stage	$-1.03\lambda^2 + 1.52\lambda - 0.20$	

Note: $\beta = \frac{h}{d}$

In the above table, h, κ and l denote the rib heights, rib width-to-spacing ratios, rib spacings, respectively.

References

[1] Murty CVR, Goel RK, Goyal A, Jain SK, Sinha R, *et al*. Reinforced concrete structures. *Earthq. Spectra*. 2002, 18:149–185.

[2] Bsisu KADI, Hunaiti Y. A comprehensive study of the seismic requirements for bond between concrete and reinforcing steel. *Adv. Mater. Res.* 2012, 446–449:490–493.

[3] Daud RA, Cunningham LS, Wang YC. Static and fatigue behaviour of the bond interface between concrete and externally bonded CFRP in single shear. *Eng. Struct.* 2015, 97:54–67.

[4] Zheng XH, Huang PY, Guo XY, Han Q. Experimental study on bonding interface between CFRP and concrete under fatigue load. *Adv. Mater. Res.* 2013, 683:381–384.

[5] Zeng JJ, Liao JJ, Zhuge Y, Guo YC, Zhou JK, *et al.* Bond behavior between GFRP bars and seawater sea-sand fiber-reinforced ultra-high strength concrete. *Eng. Struct.* 2022, 254:113787.

[6] Liao J, Zeng JJ, Bai YL, Zhang L. Bond strength of GFRP bars to high strength and ultra-high strength fiber reinforced seawater sea-sand concrete (SSC). *Compos. Struct.* 2022, 281:115013.

[7] Ahmed A, Guo S, Zhang Z, Shi C, Zhu D. A review on durability of fiber reinforced polymer (FRP) bars reinforced seawater sea sand concrete. *Constr. Build. Mater.* 2020, 256:119484.

[8] Ko H, Matthys S, Palmieri A, Sato Y. Development of a simplified bond stress-slip model for bonded FRP–concrete interfaces. *Constr. Build. Mater.* 2014, 68:142–157.

[9] Nakaba K, Kanakubo T, Furuta T, Yoshizawa H. Bond behavior between fiber-reinforced polymer laminates and concrete. *Struct. J.* 2001, 98(3):359–367.

[10] Chajes MJ, Finch WW, Thomson TA. Bond and force transfer of composite-material plates bonded to concrete. *Struct. J.* 1996, 93(2):209–217.

[11] Ferracuti B, Savoia M, Mazzotti C. Interface law for FRP-concrete delamination. *Compos. Struct.* 2007, 80(4):523–531.

[12] Eligehausen R, Popov EP, Bertero VV. Local bond stress-slip relationships of deformed bars under generalized excitations. In *Proceedings of the 7th European Conference on Earthquake Engineering*, Athens, Greece, September 20–25, 1982, pp. 69–80.

[13] Malvar LJ. Bond stress-slip characteristics of FRP rebars. 1994, pp. 1–50. Available: https://scispace.com/papers/bond-stress-slip-characteristics-of-frp-rebars-2slusqi9dq (accessed on 29 May 2025).

[14] Cosenza E, Manfredi G, Realfonzo R. Analytical modelling of bond between FRP reinforcing bars and concrete. In *Non-metallic (FRP) Reinforcement for Concrete Structures: Proceedings of the Second International RILEM Symposium*, Ghent, Belgium, August 23–25, 1995, p. 164.

[15] Yoshizawa H. Analysis of debonding fracture properties of CFS strengthened RC member subject to tension. In *the 3rd International Symposium on Non-Metallic (FRP) Reinforcement for Concrete Structures*, Sapporo, Japan, October 14–16, 1997, pp. 287–294.

[16] Japan Concrete Institute. Technical report of technical committee on retrofit technology. In *Proceedings of the JCI Symposium on the Latest Achievement of Technology and Research on Retrofitting Concrete Structures*, Tokyo, Japan, July 14, 2003, pp. 1–203.

[17] Khalifa A, Gold WJ, Nanni A, Mi AA. Contribution of externally bonded FRP to shear capacity of RC flexural members. *J. Compos. Constr.* 1998, 2(4):195–202.

[18] Malek A, Scott A, Pampanin S, Hoult NA. Postyield bond deterioration and damage assessment of RC beams using distributed fiber-optic strain sensing system. *J. Struct. Eng.* 2019, 145(4):04019007.

[19] Baky HA, Ebead UA, Neale KW. Nonlinear micromechanics-based bond–slip model for FRP/concrete interfaces. *Eng. Struct.* 2012, 39:11–23.

[20] El-Nemr A, Ahmed EA, Barris C, Joyklad P, Hussain Q, *et al.* Bond performance of fiber reinforced polymer bars in normal- and high-strength concrete. *Constr. Build. Mater.* 2023, 393:131957.

[21] Achillides Z, Pilakoutas K. Bond behavior of fiber reinforced polymer bars under direct pullout conditions. *J. Compos. Constr.* 2004, 8(2):173–181.

[22] Sólyom S, Di Benedetti M, Balázs GL. Effect of surface characteristics of FRP bars on bond behavior in concrete. *ACI SP* 2018, 327:41.1–41.20.

[23] Zhao Y, Zhang Y, Yu P, Xu J. Bond behavior of BFRP bars in concrete under lateral pressure. *Polym. Compos.* 2021, 42(11):6080–6093.

[24] Baena M, Torres L, Turon A, Barris C. Experimental study of bond behaviour between concrete and FRP bars using a pull-out test. *Compos. Part B Eng.* 2009, 40(8):784–797.

[25] Lee JY, Kim TY, Kim TJ, Yi CK, Park JS, *et al*. Interfacial bond strength of glass fiber reinforced polymer bars in high-strength concrete. *Compos. Part B Eng.* 2007, 39(2):258–270.

[26] Cosenza E, Manfredi G, Realfonzo R. Behavior and modeling of bond of FRP rebars to concrete. *Constr. Build. Mater.* 1997, 11:40–51.

[27] Ahmad FS, Foret G, Le Roy R. Bond between carbon fiber-reinforced polymer (CFRP) bars and ultra-high-performance fibre reinforced concrete (UHPFRC): experimental study. *Constr. Build. Mater.* 2010, 25(2):479–485.

[28] Yoo SJ, Hong SH, Yoon YS. Bonding behavior and prediction of helically ribbed CFRP bar embedded in ultra-high-performance concrete (UHPC). *Case Stud. Constr. Mater.* 2023, 19:e02253.

[29] Tighiouart B, Benmokrane B, Gao D. Investigation of bond in concrete member with fibre reinforced polymer (FRP) bars. *Constr. Build. Mater.* 1998, 12:453–462.

[30] Xie J, Liu Y, Qiao Y, Yan JB. Bond behaviors of ribbed CFRP bars in concrete exposed to low temperatures. *Constr. Build. Mater.* 2022, 341:127910.

[31] Yoo SJ, Yuan TF, Choi JS, Yoon YS. Comparative bond-slip response of ribbed CFRP bar to UHPC after exposure to high temperature. *Constr. Build. Mater.* 2023, 400:132583.

[32] Altalmas A, El Refai A, Abed F. Bond degradation of basalt fiber-reinforced polymer (BFRP) bars exposed to accelerated aging conditions. *Constr. Build. Mater.* 2015, 81:162–171.

[33] Yan F, Lin Z. Bond durability assessment and long-term degradation prediction for GFRP bars to fiber-reinforced concrete under saline solutions. *Compos. Struct.* 2017, 161:393–406.

[34] Basaran B, Kalkan I. Development length and bond strength equations for FRP bars embedded in concrete. *Compos. Struct.* 2020, 251:112662.

[35] Basaran B, Kalkan I. Investigation on variables affecting bond strength between FRP reinforcing bar and concrete by modified hinged beam tests. *Compos. Struct.* 2020, 242:112185.

[36] Zhao X, Rahman MM, D'Antino T, Focacci F, Carloni C. Effect of bonded length on the load response and failure mode of pull-out tests of GFRP bars embedded in concrete. *Constr. Build. Mater.* 2022, 347:128425.

[37] Wei J, Ke L, Wang P, Wang P, Li W, *et al*. Microstructure, mechanical properties and interaction mechanism of seawater sea-sand engineered cementitious composite (SS-ECC) with glass fiber reinforced polymer (GFRP) bar. *Compos. Struct.* 2024, 343:118302.

[38] Shen D, Ojha B, Shi X, Zhang H, Shen J. Bond stress-slip relationship between basalt fiber-reinforced polymer bars and concrete using a pull-out test. *J. Reinf. Plast. Compos.* 2016, 35(9):747–763.

[39] Gong Y, Song J, Zhang Y. The interfacial bond properties and model for basalt fiber reinforced polymer bar in ultra-high-performance concrete subjected monotonic and reversed cyclic loading. *J. Build. Eng.* 2023, 72:106606.

[40] Akbas TT, Celik OC, Yalcin C. Experimental investigation of bond behavior of roughened CFRP bars in high strength concrete. In *16th European Conference on Earthquake Engineering*, Thessaloniki, Greece, June 18–21, 2018, pp. 18–21.

[41] Zhang W, Tang Z. Numerical modeling of response of CFRP–concrete interfaces subjected to fatigue loading. *J. Compos. Constr.* 2021, 25(5):04021043.

[42] Rolland A, Quiertant M, Khadour A, Chataigner S , Benzarti K, *et al*. Experimental investigations on the bond behavior between concrete and FRP reinforcing bars. *Constr. Build. Mater.* 2018, 173:136–148.

[43] Lee JY, Kim KH, Kim SW, Chang M. Strength degradation of glass fiber reinforced polymer bars subjected to reversed cyclic load. *Strength Mater.* 2014, 46(2):235–240.

[44] Akbas TT, Celik OC, Yalcin C, Ilki A. Monotonic and cyclic bond behavior of deformed CFRP bars in high strength concrete. *Polymers* 2016, 8(6):211.

[45] Xie F, Tian W, Diez P, Zlotnik S, Gonzalez AG. Bonding performance of glass fiber-reinforced polymer bars under the influence of deformation characteristics. *Polymers* 2023, 15(12):2604.

[46] Liu X, Wang X, Xie K, Wu Z, Li F. Bond behavior of basalt fiber-reinforced polymer bars embedded in concrete under mono-tensile and cyclic loads. *Int. J. Concr. Struct. Mater.* 2020, 14(3):329–343.

[47] Ren Y, Wang H, Guan Z, Yang K. Evaluation of the properties and applications of FRP bars and anchors: a review. *Rev. Adv. Mater. Sci.* 2023, 62(1):20220287.

[48] ASTM International. Standard test method for tensile properties of fiber reinforced polymer matrix composite bars (ASTM D7205/D7205M-06R16). 2016, pp. 1–13. Available: https: //store. astm. org/d7205_ d7205m- 06r16. html (accessed on 10 June 2025).

[49] Ministry of Construction of the People's Republic of China and State Administration for Market Regulation. Standard for test methods of concrete physical and mechanical properties (in Chinese). 2019, pp. 1–148. Available: https://www.doc88.com/p-7884725357290.html (accessed on 10 June 2025).

[50] Ministry of Construction of the People's Republic of China and State Administration for Market Regulation. Standard of test methods of concrete structures (in Chinese). 2012, pp. 1–119. Available: https://www.doc88.com/p-1853530703278.html (accessed on 10 June 2025).

[51] Chen F, Li B, Li D, Jin L, Du X. Bond stress-slip relationship of CFRP bar–concrete interface of CFRP reinforced concrete subjected to reversed cyclic loading. *Eng. Struct.* 2024, 314:118231.

[52] Zhao J, Li X, Zhang X. Experimental and theoretical research on bond performance between CFRP bar and concrete under monotonic and reversed cyclic loading. *Eng. Struct.* 2021, 246:112994.

[53] Shen D, Wen C, Zhu P, Li M, Ojha B, *et al*. Bond behavior between basalt fiber-reinforced polymer bars and concrete under cyclic loading. *Constr. Build. Mater.* 2020, 258:119518.

[54] De Lorenzis L, Lundgren K, Rizzo A. Anchorage length of near-surface mounted fiber-reinforced polymer bars for concrete strengthening—experimental investigation and numerical modeling. *ACI Struct. J.* 2004, 101(2):269–278.

[55] Wisnom MR. Size effects in the testing of fibre-composite materials. *Compos. Sci. Technol.* 1999, 59(13):1937–1957.

[56] Lv X, Yu Z, Shan Z. Bond stress-slip model for rebar-concrete interface under monotonic and cyclic loading. *Structures* 2021, 34:498–506.

[57] Cai B, Tong J, Fu F. Bond performance of concrete reinforced with FRP bars under monotonic and fatigue loading. *Proc. Inst. Civ. Eng. Struct. Build.* 2024, 178(1):27–46.

[58] Nanni A. Guide for the design and construction of concrete reinforced with FRP bars (ACI 440.1R-03). In *Structures Congress 2005: Metropolis and Beyond*, New York, USA, April 20–24, 2005, pp. 1–6.

[59] Pilakoutas K, Guadagnini M, Neocleous K, Matthys S. Design guidelines for FRP reinforced concrete structures. *Proc. Inst. Civ. Eng. Struct. Build.* 2011, 164(4):255–263.

[60] Harajli MH. Bond stress-slip model for steel bars in unconfined or steel, FRC, or FRP confined concrete under cyclic loading. *J. Struct. Eng.* 2009, 135(5):509–518.

[61] Zhang YB, Zheng SS, Dong LG, Zheng Y. Bond behavior of corroded reinforcements in concrete: an experimental study and hysteresis model. *Arch. Civ. Mech. Eng.* 2023, 23(2):95.

[62] Nepomuceno E, Sena-Cruz J, Correia L, D'Antino T. Review on the bond behavior and durability of FRP bars to concrete. *Constr. Build. Mater.* 2021, 287:123042.

[63] Lee JY. Bond behaviour of GFRP bars in high-strength concrete: bar diameter effect. *Mag. Concr. Res.* 2017, 69(11):541–554.

[64] Mirdarsoltany M, Abed F, Homayoonmehr R, Alavi Nezhad Khalil Abad SV. A comprehensive review of the effects of different simulated environmental conditions and hybridization processes on the mechanical behavior of different FRP bars. *Sustainability* 2022, 14(14):8834.

[65] Solyom S, Balázs GL. Bond of FRP bars with different surface characteristics. *Constr. Build. Mater.* 2020, 264:119839.

[66] Li YL, Zhao XL, Singh RKR, Al-Saadi S. Tests on seawater and sea sand concrete-filled CFRP, BFRP and stainless-steel tubular stub columns. *Thin-Walled Struct.* 2016, 108:163–184.

[67] Zhou Y, Zheng B, Zhao D, Dang L, Sui L, *et al*. Cyclic bond behaviors between corroded steel bar and concrete under the coupling effects of hoop FRP confinement and sustained loading. *Compos. Struct.* 2019, 224:110991.

[68] Malavi-Fard H, Marzouk H. Bond behavior of high strength concrete under reversed pull-out cyclic loading. *Can. J. Civ. Eng.* 2002, 29(2):191–200.

[69] Xu S, Li A, Wang H. Bond properties for deformed steel bar in frost-damaged concrete under monotonic and reversed cyclic loading. *Constr. Build. Mater.* 2017, 148:344–358.

[70] Malavi-Fard H, Marzouk H. Bond behavior of high strength concrete under reversed pull-out cyclic loading. *Can. J. Civ. Eng.* 2002, 29(2):191–200.

[71] Xu S, Li A, Wang H. Bond properties for deformed steel bar in frost-damaged concrete under monotonic and reversed cyclic loading. *Constr. Build. Mater.* 2017, 148:344–358.